NAVAL POSTGRADUATE SCHOOL

MONTEREY, CALIFORNIA

THESIS

WAVE AND CURRENT OBSERVATIONS IN A TIDAL INLET USING GPS DRIFTER BUOYS

by

Stephen A. McIntyre

March 2013

Thesis Advisor: Thomas H.C. Herbers
Second Reader: Tim T. Janssen

Approved for public release; distribution is unlimited

THIS PAGE INTENTIONALLY LEFT BLANK

REPORT DOCUMENTATION PAGE			*Form Approved OMB No. 0704–0188*
Public reporting burden for this collection of information is estimated to average 1 hour per response, including the time for reviewing instruction, searching existing data sources, gathering and maintaining the data needed, and completing and reviewing the collection of information. Send comments regarding this burden estimate or any other aspect of this collection of information, including suggestions for reducing this burden, to Washington headquarters Services, Directorate for Information Operations and Reports, 1215 Jefferson Davis Highway, Suite 1204, Arlington, VA 22202–4302, and to the Office of Management and Budget, Paperwork Reduction Project (0704–0188) Washington DC 20503.			
1. AGENCY USE ONLY ***(Leave blank)***	**2. REPORT DATE** March 2013	**3. REPORT TYPE AND DATES COVERED** Master's Thesis	
4. TITLE AND SUBTITLE WAVE AND CURRENT OBSERVATIONS IN A TIDAL INLET USING GPS DRIFTER BUOYS		**5. FUNDING NUMBERS**	
6. AUTHOR(S) Stephen A. McIntyre			
7. PERFORMING ORGANIZATION NAME(S) AND ADDRESS(ES) Naval Postgraduate School Monterey, CA 93943–5000		**8. PERFORMING ORGANIZATION REPORT NUMBER**	
9. SPONSORING /MONITORING AGENCY NAME(S) AND ADDRESS(ES) N/A		**10. SPONSORING/MONITORING AGENCY REPORT NUMBER**	
11. SUPPLEMENTARY NOTES The views expressed in this thesis are those of the author and do not reflect the official policy or position of the Department of Defense or the U.S. Government. IRB Protocol number ____N/A____.			
12a. DISTRIBUTION / AVAILABILITY STATEMENT Approved for public release; distribution is unlimited		**12b. DISTRIBUTION CODE**	

13. ABSTRACT (maximum 200 words)

The Wave Resolving Drifter (WRD) Buoy, developed at NPS, was refined by adding an accelerometer and utilizing horizontal Doppler velocity measurements to better resolve the wave surface motions. The WRD Buoy was validated against a Datawell Waverider-GPS buoy by comparing bulk wave statistics, wave energy spectra and wave directional spectra. The validation was performed in deep water, offshore of Monterey Bay, CA. Horizontal measurements from Doppler velocities showed improved capability, particularly in the wind-wave band. Vertical measurements were significantly improved through the addition of the accelerometer. A large array of WRD buoys was deployed in the Golden Gate channel at the entrance to San Francisco Bay and allowed to drift with the outgoing ebb current. The simultaneous deployment of many drifters provides a unique view of the details of the temporal and spatial evolution of the wave field as it propagated through regions of bathymetric and wave-current interactions. Wave heights increased as the wave field propagated over the ebb-tidal shoal and at the entrance to the channel, in the presence of a strong opposing ebb current, as expected. Inside the channel, strong dissipation of high frequency wind waves was observed in the opposing current.

14. SUBJECT TERMS Ocean waves, Tidal currents, Wave buoys, GPS, Accelerometer, Ebb-tidal shoal, Wave-bathymetry interaction, Wave-current interaction			**15. NUMBER OF PAGES** 99
			16. PRICE CODE
17. SECURITY CLASSIFICATION OF REPORT Unclassified	**18. SECURITY CLASSIFICATION OF THIS PAGE** Unclassified	**19. SECURITY CLASSIFICATION OF ABSTRACT** Unclassified	**20. LIMITATION OF ABSTRACT** UU

NSN 7540–01–280–5500 Standard Form 298 (Rev. 2–89)
Prescribed by ANSI Std. 239–18

THIS PAGE INTENTIONALLY LEFT BLANK

Approved for public release; distribution is unlimited

WAVE AND CURRENT OBSERVATIONS IN A TIDAL INLET USING GPS DRIFTER BUOYS

Stephen A. McIntyre
Lieutenant Commander, United States Navy
B.S., Auburn University, 2002
M.S., University of Southern Mississippi, 2009

Submitted in partial fulfillment of the
requirements for the degree of

MASTER OF SCIENCE IN METEOROLOGY AND OCEANOGRAPHY

from the

NAVAL POSTGRADUATE SCHOOL
March 2013

Author: Stephen A. McIntyre

Approved by: Thomas H.C. Herbers
Thesis Advisor

Tim T. Janssen
Second Reader

Peter C. Chu
Chair, Department of Oceanography

THIS PAGE INTENTIONALLY LEFT BLANK

ABSTRACT

The Wave Resolving Drifter (WRD) Buoy, developed at NPS, was refined by adding an accelerometer and utilizing horizontal Doppler velocity measurements to better resolve the wave surface motions. The WRD Buoy was validated against a Datawell Waverider-GPS buoy by comparing bulk wave statistics, wave energy spectra and wave directional spectra. The validation was performed in deep water, offshore of Monterey Bay, CA. Horizontal measurements from Doppler velocities showed improved capability, particularly in the wind-wave band. Vertical measurements were significantly improved through the addition of the accelerometer. A large array of WRD buoys was deployed in the Golden Gate channel at the entrance to San Francisco Bay and allowed to drift with the outgoing ebb current. The simultaneous deployment of many drifters provides a unique view of the details of the temporal and spatial evolution of the wave field as it propagated through regions of bathymetric and wave-current interactions. Wave heights increased as the wave field propagated over the ebb-tidal shoal and at the entrance to the channel, in the presence of a strong opposing ebb current, as expected. Inside the channel, strong dissipation of high frequency wind waves was observed in the opposing current.

THIS PAGE INTENTIONALLY LEFT BLANK

TABLE OF CONTENTS

LIST OF FIGURES

THIS PAGE INTENTIONALLY LEFT BLANK

LIST OF TABLES

THIS PAGE INTENTIONALLY LEFT BLANK

LIST OF ACRONYMS AND ABBREVIATIONS

C/A-code	Coarse Acquisition Code
DoD	Department of Defense
DWR-G	Datawell Waverider – GPS Buoy
FFT	Fast Fourier Transform
GPS	Global Positioning System
H/P/R	Heave Pitch Roll Buoy
MEMS	Micro-Electro-Mechanical System
MRU	Motion Reference Unit
NDBC	National Data Buoy Center
NOAA	National Oceanic and Atmospheric Administration
P-code	Precision Code
R/V	Research Vessel
SA	Selective Availability
SBAS	Space Based Augmentation System
SWAN	Simulating Waves Nearshore
WAM	Wave Action Model
WRD	Wave Resolving Drifter Buoy

THIS PAGE INTENTIONALLY LEFT BLANK

ACKNOWLEDGMENTS

I would like to sincerely thank Professor Tom Herbers for his guidance and help over the past two years in conducting this research and expanding my knowledge of nearshore wave processes. His expertise and vision are true assets not only for the continued academic excellence of the Naval Postgraduate School, but also to the continued and impactful research of nearshore ocean processes.

I would also like to thank Mr. Paul Jessen and LT Doug Pearman for their friendship, engineering prowess, and Matlab tutorials over the past two years. The field work conducted for this research was an awesome opportunity, and the many cruises up to San Francisco were a welcome distraction from the classroom; as well as a lot of fun.

I would like to thank Dr. Tim Janssen for his continued support and assistance throughout the development of this study. His expertise in wave-current interactions was instrumental in the continued the development of these GPS drifters. Additionally, he arranged the support of R/V Questuary, from San Francisco State University, which enabled the deployment of the GPS drifters in the Golden Gate channel.

The crew of the R/V Point Sur was extremely professional and accommodating during all four of our research cruises. They provided much needed help while chasing countless drifting buoys all around San Francisco Bay in the middle of the night. Trips to sea with them definitely made me miss the days of being underway.

Finally, I would like thank my family for their continued love and support not only while here at NPS, but throughout my naval career. Although I always seem to be on the other side of the country, their support has enabled me to achieve everything I set out to do.

THIS PAGE INTENTIONALLY LEFT BLANK

I. INTRODUCTION

A. NEARSHORE WAVE PROCESSES

Wind-generated surface waves are present on every body of water. In the open ocean their properties depend on the wind speed, duration and fetch length. Higher wind speeds, longer durations and longer fetches all result in larger wind-generated waves. However, in the nearshore environment, wave properties are also affected by interactions with bathymetry, tides and surface currents. These nearshore features can alter a wave field's amplitude, speed and direction of propagation.

The primary influence on nearshore wave behavior is the effect from bathymetry. As deep-water waves propagate into the nearshore environment, the water depth decreases and begins to affect the propagation speed, amplitude and direction. This effect is most evident near the beach where shoaling bathymetry slows down the approaching waves causing the wave amplitude and steepness to increase resulting in the breaking wave observed in the surf zone. The variable nearshore bathymetry also interacts with wave propagation by refracting the wave crest, altering the wave's direction of propagation. This refraction process typically causes a focusing of wave energy on sand bars and coastal headlands.

A second influence on nearshore wave behavior is that of tides. Ocean tides are most noticeable in the swash zone on the beach where the water level moves forward and backward throughout the day. Tides are described by three categories based on their frequency and variability: diurnal, semidiurnal, or mixed (see Figure 1). The frequency and characteristics of the tide are controlled by a combination of harmonic tidal constituents and vary based on location. Mixed tides, most common on the west coast of the U.S., experience two high tides and two low tides per day, with one of each being larger than the other. The large tidal movement of water into and out of an inlet can drive strong currents. Ebb currents (flowing out of a bay) and flood currents (flowing into a bay) can be extremely strong, particularly in narrow tidal inlets depending on the tidal

range and the size of the bay. These tidally-generated currents can affect the propagation speed of a wave, thus altering the wave properties in a manner similar to the shoaling and refraction effects of variable depth.

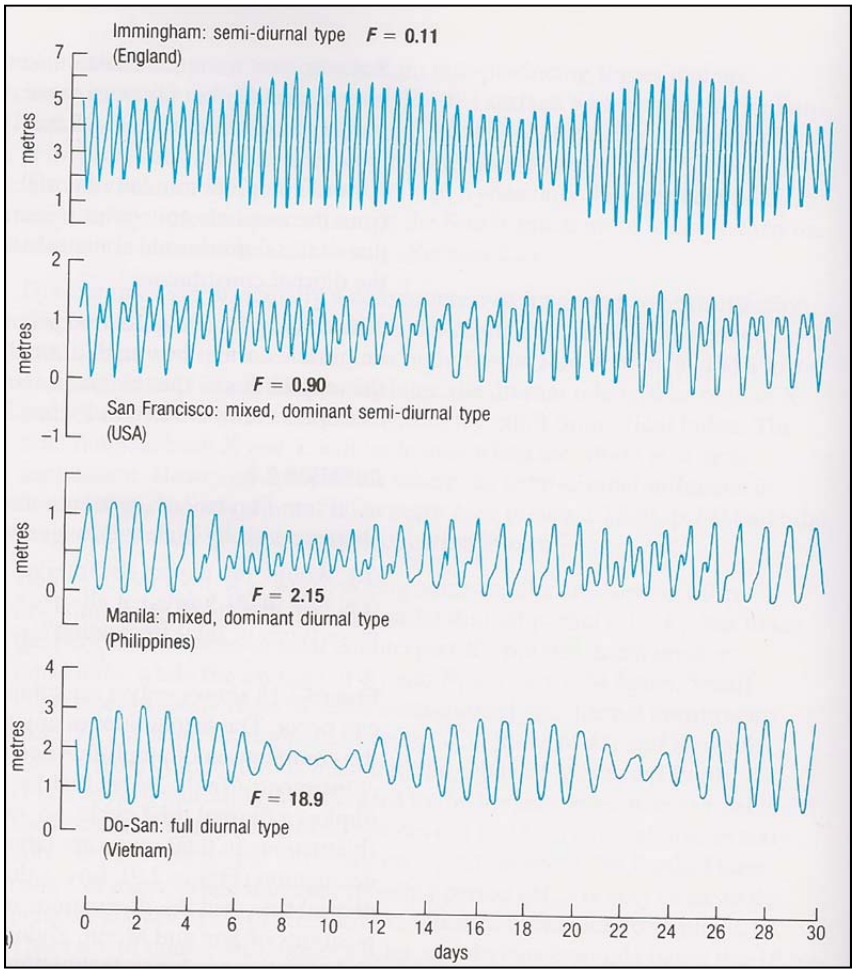

Figure 1. Examples of tide characteristics (Fig (2.18a) in Open University 1999).

In addition to the characteristics of the daily fluctuations, relative tidal strengths also observe a cyclical oscillation based on the lunar cycle. Spring tides occur twice per month coinciding with the celestial alignment of the sun, earth and moon. This results in the largest intra-daily differences in high tide and low tide. These large tidal differences result in the strongest tidally-generated currents. Conversely, neap tides occur when the sun, earth and moon are offset by 90° resulting in the smallest intra-daily difference between high tide and low tide, and accordingly weaker tidally-generated currents.

Other surface currents also affect nearshore wave behavior. Nearshore wind and wave-driven currents typically flow alongshore and generate eddy circulations and rip currents depending on local bathymetric features. These surface currents and circulations interact with approaching wave fields.

The variability in direction and strength of currents can have direct impacts on the evolution and propagation of a wave field. An opposing surface current will tend to amplify wave heights at focal regions due to the refraction of wave energy about the current (Wolf and Prandle 1999). This situation can result in variable wave heights and directions in regions of strong wave-current interactions.

These combined effects of bathymetry, tides and surface currents in the nearshore environment can result in large and abnormal wave conditions making ocean wave measurements difficult. Although traditional Eulerian measurements remain ideal for providing a robust time series of wave measurements at a specific location, they are not ideal for capturing the spatial variability which is often seen in the nearshore environment. A large array of fixed instruments or moored buoys would need to be deployed to capture such spatial variability, which is cost prohibitive. Additionally, heavy shipping channels pose a hazard to moored buoys where the buoys might sustain damage and accessibility for maintenance is restricted. The moorings themselves can also be negatively impacted in a dynamic nearshore environment, particularly in areas with rapidly changing bathymetry or extreme surface currents which can put undue strain on the moorings. On the other hand, drifting wave buoys that follow along with the surface current are able to capture both the temporal and spatial variability across this dynamic environment. Recent advances in inexpensive instrumentation have enabled the deployment of a large array of cost-effective buoys that are capable of observing the temporal and spatial evolution of the wave field across the nearshore environment. These large arrays of drifter buoys have the potential to provide accurate and reliable wave measurements in this dynamic environment which are essential for the improvement and validation of nearshore numerical models.

Over the past five decades, various models have been developed to characterize and predict ocean waves such as WAM (Wave Action Model) and WAVEWATCH III. These models invariably assume Gaussian and homogeneous statistics and perform well in deep-water environments where the wave statistics are relatively weakly nonlinear and slowly varying. For nearshore applications, wave models such as SWAN (Simulating Waves Nearshore) or coupled wave-current-transport models such as DELFT-3D have evolved to accurately capture wave-current and wave-bathymetry interactions. However, accurate field observations that are required to initialize and validate these models are scarce.

B. APPLICABILITY OF LINEAR WAVE THEORY

Numerical wave prediction models and techniques for the analysis of ocean wave observations are often based on the principles of linear wave theory. This theory simplifies the solution to the wave equation by assuming that the wave amplitude is much smaller than both the wavelength and the water depth. The first-order solution for a sinusoidal wave obeys a linear dispersion relationship relating the wave frequency (ω), the wavenumber (k) and the water depth (H):

$$\omega^2 = gk \tanh\left(kH\right) \tag{1}$$

This linearized theory also gives approximate solutions for wave-induced fluid motions at and below the surface, and the associated pressure field. The accuracy of linear wave theory is well established. Thornton and Krapohl showed that measured wave orbital velocity fluctuations can be related to sea surface height through linear wave theory (1974). Herbers et al. (1992) demonstrated that the linear transfer functions between wave orbital velocities and bottom pressure (wave height) are accurate to within a few percent.

The robustness of linear wave theory has led the way for a variety of in-situ instruments and remote sensing platforms than can be used for observing ocean waves with varying degrees of accuracy, resolution, and spatial/temporal coverage.

C. OCEAN WAVE SENSING STRATEGIES

Early sensors include simple tide staffs that can be deployed at any location to observe the instantaneous sea surface height, but this is a much localized and manual measurement. Radar altimeters deployed onboard aircraft and satellites are capable of providing wave height measurements based on the differential reflection of a radar pulse from the crest and trough of a wave (Stewart 2008). The satellite-based altimeter is ideal for observing a large area over a long period of time, but does not resolve the detailed wave motion. Coastal surface-based radars have been used for measuring ocean waves based on Bragg scattering from small-scale roughness elements on the sea surface. Similar to altimeters, these sensors are ideal for long-period observations, but are restricted to local, coastal regions, and their wave height measurements are frequency-dependent (McWilliams 2005). Additionally, the transfer functions between the radar back scatter and the surface wave heights are less well understood. Pressure sensors have been developed that are capable of observing the pressure differential of passing waves. These bottom-mounted sensors are extremely portable and ideal for deploying in a desired location; however, they are restricted to shallow water depths in order to avoid the attenuation of the "wave-induced pressure fluctuations" (Stewart 2008). Similar to pressure sensors, ocean current meters have been developed that are capable of observing wave heights through the changing water particle velocities associated with passing waves, but these sensors also only provide localized measurements (Thornton and Krapohl 1974).

Still, the most common sensor for measuring wave heights has been the wave buoy, which physically observes the change in sea surface elevation. Wave buoys can either be moored in a specific location or allowed to drift with the current. The first generation of wave buoys relied on heave, pitch and roll measurements in order to determine the wave height and sea surface slope (H/P/R buoys). These measurements were made by accelerometers integrated into a motion reference unit (MRU). The vertical accelerations (heave measurements) were used to calculate the wave height, while the pitch and roll measurements were used to calculate the sea surface slope. Through the combination of the "vertical accelerations and the slope of the water surface…the

directional spectrum [was] estimated" (Long 1980). A modern example of an H/P/R buoy is the NOAA discus buoy (see Figure 2) (Krogstad 2003).

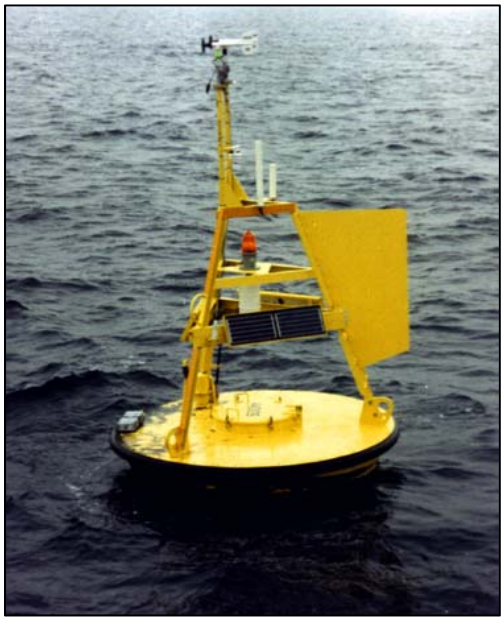

Figure 2. A NOAA 3m H/P/R discus buoy (From http://www.ndbc.noaa.gov/images/buoys/3m.jpg).

Further improvements to H/P/R buoys introduced a magnetic compass for heading as well as advancements in the accelerometers. Similar to the H/P/R buoys, these displacement buoys measured the wave height from vertical accelerations; however, the wave direction was obtained from a combination of the compass heading and horizontal accelerations. A modern example of these buoys is the Datawell Waverider buoy (see Figure 3) (Krogstad 2003).

Figure 3. A 0.9m Datawell Waverider displacement buoy (From http://www.datawell.nl/inhoud.php?id=3).

The most recent improvement to wave buoys was the addition of Global Positioning System (GPS) receivers (Krogstad 2003). Although GPS accuracy has varied, this step provided a direct measurement of both the wave height and wave direction from the vertical and horizontal displacements of the buoy. Continued improvements to the accuracy of GPS receivers have provided increasingly accurate measurements of buoy displacements, allowing for long distance tracking of the buoys. Improvements have also been made to the GPS sensing strategy reducing the size and cost of the GPS receivers (Herbers et al. 2012). The development of inexpensive GPS drifter buoys shows promise for deployments in large numbers to map the evolution of waves and surface currents.

D. GPS BACKGROUND

The evolution and accuracy of the GPS system is central to its employment in modern wave buoys used in this study. The GPS System is a passive, satellite-based positioning system originally designed for use by the Department of Defense (DoD) and the U.S. military, currently consisting of 36 active positioning satellites. These satellites transmit a coded signal that is received by a receiver on Earth. The travel time of the

coded signal is used to determine the range to the satellite – referred to as pseudo-ranging. The receiver uses pseudo-ranges from multiple satellites in order to triangulate its position on Earth (see Figure 4). Since satellite signals require a line of sight, they are only visible in a 180° hemispheric viewpoint. This underlying geometry provides for greater accuracy in the horizontal plane than in the vertical plane (El Rabbany 2006).

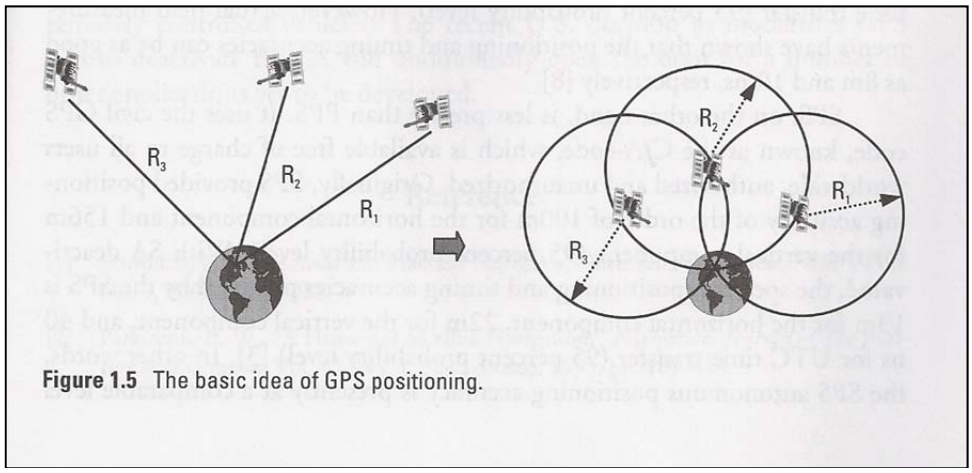

Figure 4. The principle of positioning through trilateration (Fig (1.5) in El-Rabbany 2006).

The coded signal transmitted by the GPS satellite contains one of two binary codes. Low-cost commercial GPS receivers are typically single-frequency receivers that are capable of only receiving the coarse-acquisition code (C/A-code). The length and repetition rate of this code results in a real-time positioning resolution of 300m. More expensive survey-grade GPS receivers are typically dual-frequency receivers which can receive both the C/A-code and the precision code (P-code). The length and higher repetition rate of the P-code allows for real-time positioning accuracies within 30m. Until 2000, the U.S. Government intentionally introduced some error into the GPS code known as selective availability (SA) in order to prevent high accuracy real-time positioning by commercial and non-military GPS receivers. This function has since been deactivated and the accuracy of the C/A-code has returned to 300m (El Rabbany 2006).

The GPS signals are used to for real-time positioning by one of two techniques: code-phase or carrier-phase positioning. The code-phase positioning is the less accurate

of the two methods and involves the comparison of the receiver-generated code with the satellite-generated code, which results in pseudo-range accuracies that are dependent on the length of the code (approximately 300m or 30m). Assuming that the messages were initiated at the same time, the time delay required to synchronize the two messages corresponds to the travel time of the transmitted message, thus providing the pseudo-range to the satellite (see Figure 5). There is some error in this calculation due atmospheric propagation as well as inherent timing issues between the satellite and the receiver (El Rabbany 2006).

Carrier-phase positioning involves the measurement of the total number of sinusoidal oscillations of the carrier frequency during the transmission (see Figure 5). This results in pseudo-range accuracies that are dependent on the wavelength of the carrier signal (19cm for the L1 frequency); however, the signal is purely sinusoidal and therefore the total number of oscillations cannot be readily measured.

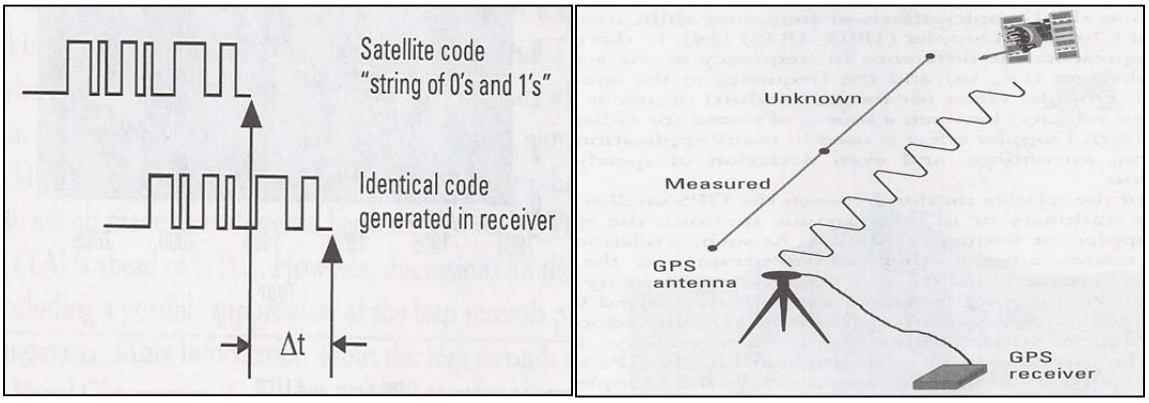

Figure 5. GPS positioning techniques. The left panel shows the concept of code-phase positioning. The right panel shows the concept of carrier-phase positioning (Fig (2.4) and Fig (2.5) in El-Rabbany 2006).

In order to improve real-time positioning accuracy of code-phase positioning, various differential correction techniques can be implemented in order to reduce some systematic errors. The most common technique is the use of a space-based augmentation system (SBAS). GPS receivers located at known geodetic positions across the country (and the world) calculate corrected pseudo-ranges to the satellites based on their known

position. These corrections are transmitted to a satellite, which are then broadcast to other GPS receivers on the ground. This improves the real-time accuracy of standard GPS receivers (300 meters) to less than tens of meters (El Rabbany 2006).

An additional improvement to modern GPS receivers is their measurement of velocity. Speed used to be measured by positional differences which contained tens of meters of uncertainty. Just as carrier-phase positioning began utilizing the characteristics of the carrier frequency, GPS receivers began measuring the Doppler shift of this frequency in order to determine the receiver's velocity. Although this doesn't provide real-time position, these measurements result in very accurate velocity measurements (within 10cm/sec) as opposed to absolute positional accuracies of tens of meters.

The improvements in low-cost GPS receivers, such as the Locosys GT-31, which utilize SBAS DGPS corrections and measure velocities through the Doppler shift of the carrier frequency, result in accurate ocean wave and current measurements. The employment of these types of GPS receivers on drifter buoys provides the ability to measure wave-induced surface motions anywhere in the world, particularly the dynamic nearshore environment (see Herbers et al. 2012).

E. ACCELEROMETER BACKGROUND

Just as GPS has advanced over recent decades, accelerometers have also evolved, providing greater accuracy at ever reducing size and cost. Originally large mechanical devices, accelerometers provide measurements of accelerations in specific directions based on the displacement of a mass. However, the development of the MEMS (micro-electro-mechanical systems) sensor has been instrumental in making accelerometers smaller, more sensitive, and reliable.

MEMS accelerometers use capacitance measurements between two surfaces to determine the acceleration of an object. A movable proof mass with extended arms is suspended on a spring between arrays of fixed arms (see Figure 6). As the accelerometer is moved, the suspended proof mass moves up or down in relation to the fixed array. This motion changes the relative distance between the arms of the suspended proof mass and the arms of the fixed array. Voltage sensors on the arms measure capacitance. The

variable capacitance measurements between the arms of the fixed array and the arms of the suspended proof mass are used to calculate the displacement of the suspended mass, and thus the acceleration (Andrejasic 2008).

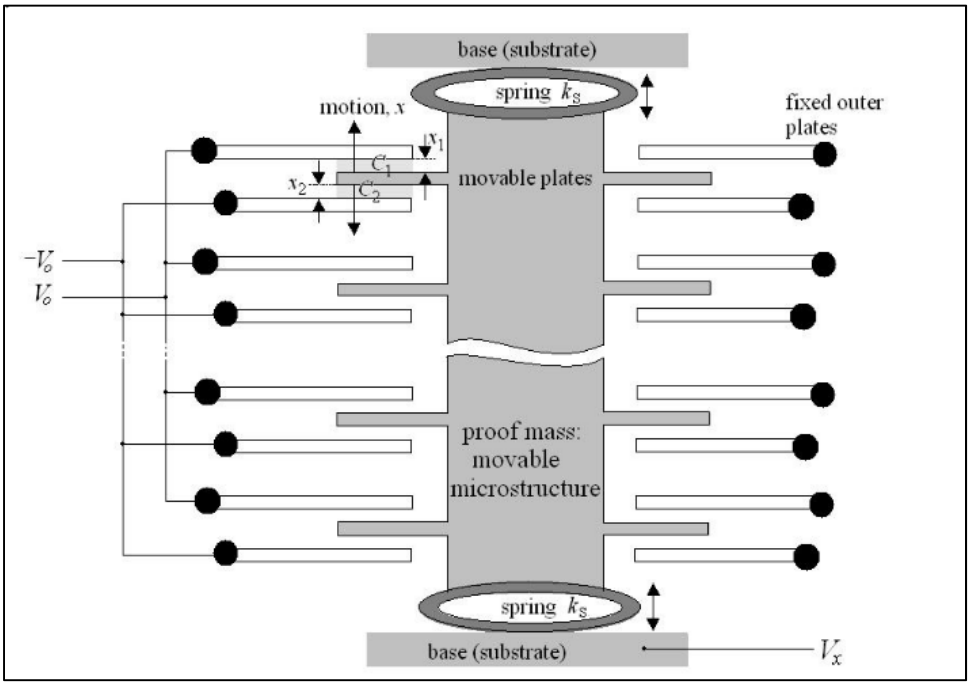

Figure 6. MEMS accelerometer design (From Andrejasic 2008).

The fundamental design of MEMS accelerometers measures both static (due to gravity) and dynamic (due to motion) accelerations, which allows these sensors to be oriented in any direction (Andrejasic 2008). Modern MEMS accelerometers have sensor plates aligned orthogonally in order to measure accelerations in all three axes (x, y, z). Since the sensors measure static as well as dynamic acceleration, the vertically-aligned axis on a multi-axis accelerometer can be identified by the measured gravitational acceleration. The reduced size and improved sensitivity of these sensors make them ideal for integration into wave buoys.

F. RESEARCH MOTIVATION

The effects of the nearshore environment on ocean waves can be extreme and result in abnormal wave conditions which are hazardous to shipping and maritime

operations. The effects of bathymetry and tidal currents around inlets have been shown to focus wave energy in specific locations, setting up strong and variable surface currents. Bathymetric features can cause wave heights to increase and waves to break resulting in potentially hazardous conditions. Strong currents can also affect safety of navigation and generate strong eddy circulations. The effects of focused wave energy and strong surface currents can combine to result in shifting sand bars, sand waves, and beach erosion. Coastal zone management agencies continually strive to understand and mitigate these effects in order to preserve coastlines, coastal habitats and civilian coastal infrastructure. Nearshore waves and currents are constantly monitored for potentially hazardous conditions that affect swimmers, shipping and small boat operations.

The U.S. Navy as well as civilian maritime agencies, continue to require safety of navigation within this dynamic nearshore environment in order to transit in and out of desired ports and harbors. This requires an accurate understanding and improved prediction capability of ocean waves. Although the accuracy of ocean wave models continues to improve, their improvement relies on the continued validation of their output and increasing accuracy of the initialization conditions. Recent research has shown the promise of using GPS wave buoys for ocean wave measurements. In this study we further refine an inexpensive GPS-tracked buoy (Herbers et al. 2012). Specifically, we add an inexpensive accelerometer to the GPS drifter buoy which provides more robust and accurate vertical surface height measurements, while maintaining a cost-effective Lagrangian drifter buoy. This buoy design is advantageous for deploying in a large array in order to accurately measure the spatial variability of wave fields in a dynamic nearshore environment.

II. FIELD EXPERIMENT AND DATA

The field experiment was conducted at two locations during four cruises onboard the R/V Point Sur. The first part of the experiment involved the continued development and validation of a new wave resolving drifter (WRD) buoy. The second part of the experiment involved the deployment of a large array of these WRD buoys in and around the entrance to San Francisco Bay, where strong tidal currents and an ebb-tidal shoal interact with the approaching ocean swell creating strong wave-current interactions.

A. BUOY VALIDATION

1. Experiment Location

The validation of the WRD buoy was performed approximately 30nm northwest of Monterey, CA (see Figure 7). The experiment was conducted from the R/V Point Sur based out of Moss Landing, CA. This validation site, well offshore of Monterey Bay in an average depth of 1700m, was selected to ensure that the surface waves were not affected by any bathymetric or coastal sheltering effects. The strong (24 mph) and steady wind out of the northwest (325°) allowed for the measurement of a fully developed wave field that was relatively homogenous in space and time. Additionally, the location was approximately 11nm from the National Data Buoy Center (NDBC) Station 46042, which provided coinciding environmental conditions.

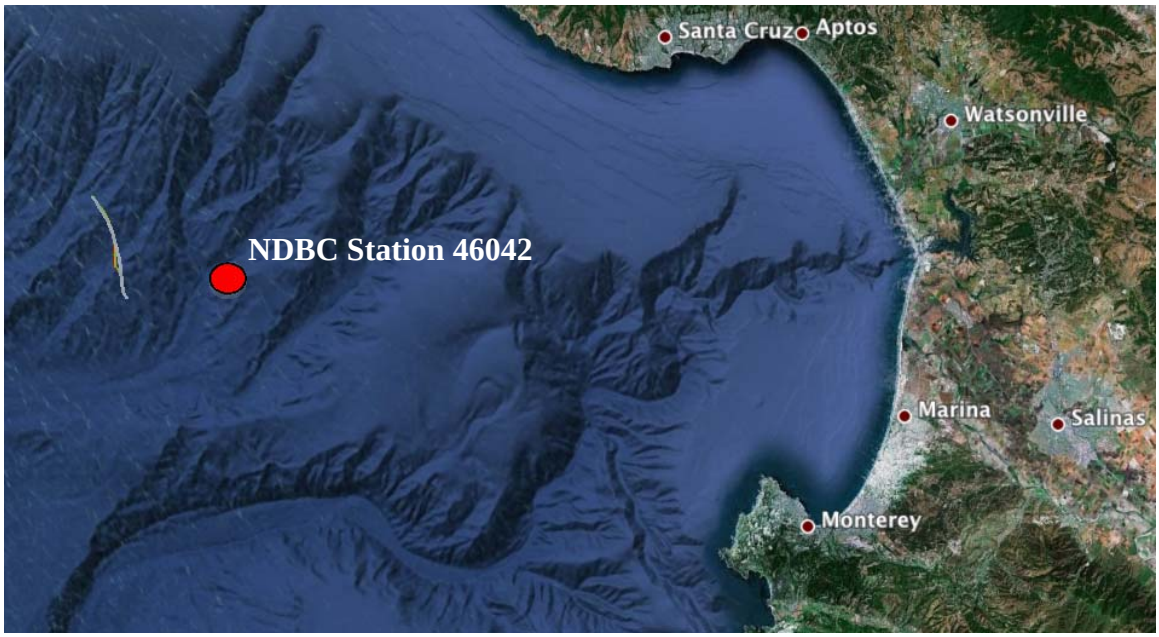

Figure 7. Drift track of the validation deployment offshore of Monterey Bay, CA. The position of NOAA Buoy 46042 is noted (From Google Earth).

The validation dataset was collected on April 29th, 2012 during one continuous eight-hour deployment. A total of four wave buoys were deployed: one Datawell Waverider buoy and three WRD buoys. The Datawell was deployed for comparison and treated as a "ground truth." The buoys were deployed simultaneously at the same location from the working deck of the R/V Point Sur, ensuring that all four buoys observed the same wave field. During the eight-hour deployment, the Datawell and WRD buoys experienced slightly different drift characteristics, and were separated by 2km by the end of the deployment.

2. Atmospheric Conditions

Local atmospheric conditions were recorded by NDBC Station 46042 which is a 3m discus buoy maintained by the National Data Buoy Center. This station provided hourly observations of atmospheric pressure, air temperature, surface wind speed (at 10m above the sea surface), surface wind direction, wave height, dominant wave period, average wave period, mean wave direction and sea surface temperature.

During the validation experiment, surface winds were out of the northwest (327°) at approximately 11m/s. The average wave height was 2.8m coming out of the northwest (310°) with a dominant wave period of 10 seconds. Hourly observations from Station 46042 on April 29, 2012 are listed in Table 1.

Table 1. Atmospheric and wave conditions reported by NDBC Buoy 46042 during the period of the validation deployment.

	Time (UTC)	Wind Dir	Wind Spd (m/s)	Gust (m/s)	Wave Dir	Wave Hgt (m)	Wave Per (sec)
Apr 29	0050	327	9.4	11.4	314	2.96	11.43
	0150	323	10.7	12.5	306	2.9	11.43
	0250	320	11.5	14.4	306	2.8	12.12
	0350	323	10.8	13.2	306	2.78	11.43
	0450	319	10.9	13.3	310	2.72	10
	0550	318	12.8	16.4	306	2.48	10.81
	0650	321	12.4	14.5	310	2.59	10.81
	0750	325	10.7	12.7	315	2.63	11.43
	0850	323	10.3	12.2	305	2.72	10.81
	0950	321	10.9	12.6	310	2.72	10.81
	1050	327	10.8	14.2	310	2.66	10.81
	1150	332	13	16	319	2.51	10.81
	1250	333	11.9	15.2	308	2.98	8.33
	1350	336	11.3	13.8	311	2.96	8.33
	1450	333	11.5	13.4	315	3.24	8.33
	1550	332	11.3	13.2	319	3.05	9.09
	1650	335	10.6	12.8	314	3.35	8.33
	1750	328	10	12.6	312	3.42	10.81
	1850	330	9.1	10.9	307	3.03	10
	1950	326	8.5	10.3	312	3.21	10.81
	2050	326	9.7	11.1	317	3.2	10.81
	2150	336	8.4	10.1	310	2.99	10.81
	2250	337	8	9.9	309	3.06	10.81
	2350	339	8.3	9.8	311	2.85	10

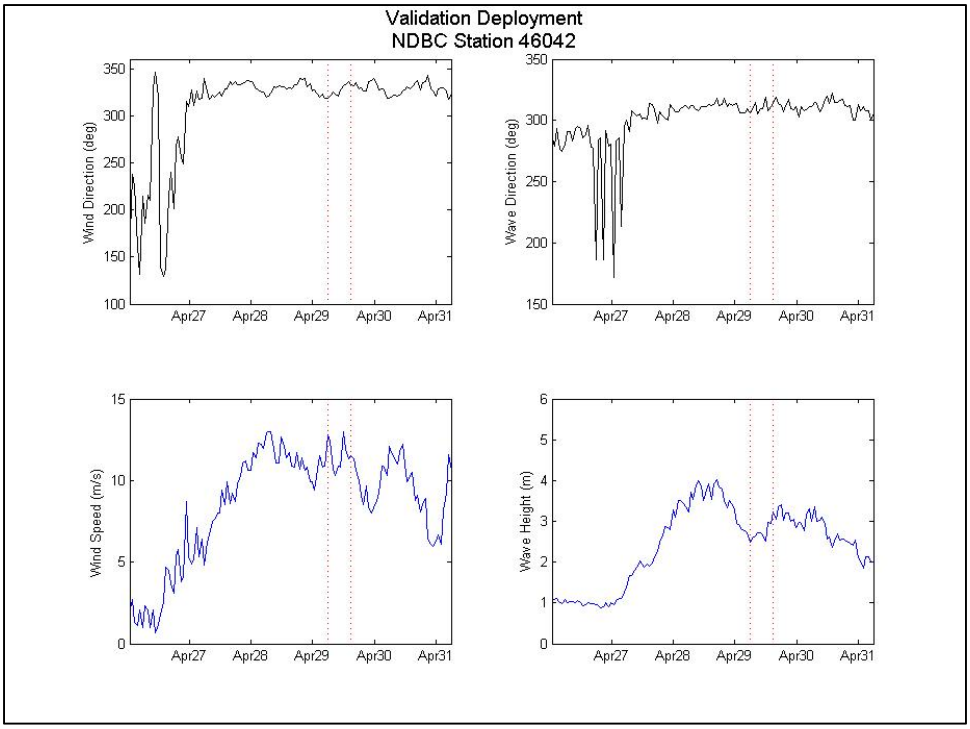

Figure 8. Wind speed and offshore wave height recorded at NDBC Station 46042 for the validation deployment.

3. Datawell DWR-G Buoy Sensors and Configuration

The Datawell was deployed as the accepted industry standard for GPS wave buoys. The model that we employed was the 0.4m diameter Datawell Waverider – GPS (DWR-G4), which retails for approximately $14,000 (see Figure 9). This buoy is constructed from stainless steel, capable of withstanding a collision and corrosion, and is specifically designed for the marine environment. The buoy utilizes Doppler velocity measurements from an integrated GPS receiver to calculate horizontal and vertical excursions. The GPS receiver is capable of resolving positional displacements of 0.01m and direction within 1.5°. The GPS receiver operates at a sampling frequency of 1.28Hz. The onboard processor utilizes a proprietary algorithm, which converts the observed horizontal and vertical position displacements into wave height spectra and directional spectra. An onboard data logger records both horizontal and vertical position

displacements as well as the computed wave height and direction spectra. The DWR-G records one full GPS fix and transmits its position once every 30 minutes (Datawell 2010).

For this experiment, the DWR-G was also outfitted with the GT-31 GPS receiver and X6–2 accelerometer described in the next section for the purpose of sensor comparison and validation (see Figures 9 and 10).

Figure 9. Datawell Waverider Buoy (DWR-G) drifting off of San Francisco Bar (left panel). DWR-G drifting off of Monterey Bay, CA (right panel).

Figure 10. DWR-G external sensor configuration (left panel). GT-31 GPS receiver is visible on the bottom left. Two GoPro cameras are attached to the top of the buoy. DWR-G internal sensor configuration (right panel). The blue X6–2 accelerometer is visible in the top left of the internal board, while a Yost accelerometer (for future testing) is visible in the center.

4. Wave Resolving Drifter (WRD) Buoy Sensors and Configuration

The WRD buoy developed at NPS is built around a 0.4m diameter Jim Buoy float and costs less than $1,000 per buoy. The WRD is outfitted with a Locosys GT-31 handheld GPS receiver and a Gulf Coast Data Systems X6–2 three-axis accelerometer. The buoys are also outfitted with a NaviSafe marine light, Merlin Systems radio transmitter and Garmin DC-40 GPS tracking collar for real-time position tracking (see Figure 11 and 12). The GT-31 GPS receiver is waterproof; however, it is secured inside a clear plastic bag for added protection in the nearshore environment. The GT-31 is secured near the top of the WRD in order to ensure optimal line-of-sight in large waves, minimizing satellite drop-outs. The X6–2 accelerometer is secured inside a watertight Otterbox case, which is attached approximately 0.3m beneath the buoy. The Otterbox case is suspended between the buoy and 20lbs of anchor chain used to ballast the buoy (see Figure 15). The anchor chain serves three purposes: it provides adequate ballast in order to ensure the centerline of the buoy rides at the water surface, it ensures the accelerometer remains consistently vertical while minimizing tilt, and it increases the submerged surface area of the buoy on which the current can act, to keep it well coupled to the surface drift.

Figure 11. Wave Resolving Drifter (WRD) drifting inside Golden Gate Channel (left panel). WRD buoys drifting off of Monterey Bay, CA (right panel).

Figure 12. WRD Buoy. GT-31 GPS receiver (front), Garmin GPS tracking collar (left), Merlin RF transmitter (right) and NaviSafe marine light (back) are mounted externally on the buoy.

a. Locosys GT-31 GPS Receiver

The Locosys GT-31 is a single-frequency, handheld GPS receiver that costs approximately $135 (see Figure 13). This GPS receiver was previously used on earlier versions of GPS drifters developed for offshore wave observations (Herbers et al. 2012). The unit utilizes a built-in patch antenna and lithium-ion polymer battery making it compact and portable. The battery is capable of 41 hours of continuous operation allowing it be used for day-long deployments. The receiver operates on the L1 carrier frequency, utilizing the C/A-code for pseudo-ranging. Additionally, the GPS receiver receives DGPS corrections via a space-based augmentation system (SBAS) allowing for greatly improved pseudo-ranging and positioning. The sampling frequency of the receiver is 1Hz (Locosys 2007).

The GPS receiver records measured horizontal and vertical displacements in meters with an uncorrected accuracy within ten meters. The receiver also measures the Doppler shift of the carrier frequency providing velocity measurements accurate within 0.1m/s (Locosys 2007). Raw data is stored internally on a 2GB SanDisk SD card allowing for autonomous operation.

Figure 13. GT-31 GPS receiver.

b. X6–2 Accelerometer

The Gulf Coast Data Concepts (GCDC) X6–2 is a three-axis accelerometer that costs approximately $115. The accelerometer is extremely small, slightly larger than an average thumb drive and weighs only 1.3oz (see Figure 14). The accelerometer contains an internal lithium-polymer battery that is capable of 36 hours of continuous operation at the highest sampling frequency (320Hz) allowing it to be used for day-long deployments. The sampling frequency is adjustable and set to 10Hz for this experiment, providing much longer battery life. The accelerometer is capable of measuring accelerations up to 6g with an accuracy of 0.004g in the horizontal (X and Y directions) and 0.006g in the vertical (Z direction) (Gulf Coast Data Concepts 2010).

Figure 14. X6–2 accelerometer.

Figure 15. Tethered configuration of the X6–2 accelerometer. The X6–2 is secured inside a waterproof Otterbox and is ballasted by 20lbs. of chain link.

c. Real-time Position Tracking

Three different devices were implemented in order to aid in the real-time position tracking of the WRD buoys. Every WRD buoy was outfitted with a NaviSafe marine light, which cost approximately $70. The marine light was installed in order to aid in visibility and location of the buoys at night.

Every WRD buoy was also outfitted with a small Merlin 1/3N MX transmitter that costs approximately $160 (see Figure 16). This transmitter was enclosed in a waterproof case that was sealed into the top of the WRD buoy. Each transmitter emits a unique radio signal between 216 and 219MHz at one second intervals. The MS-1000 Multi-Channel receiver was used for radio direction finding, providing coarse tracking and recovery.

Figure 16. The left panel shows the Merlin 1/3N MX radio transmitter. The right panel shows the MS-1000 Multi-Channel receiver used for radio direction finding (From http://www.merlin-systems.com).

The Garmin DC-40 GPS tracking collar was attached to many WRD buoys and costs approximately $200. The GPS unit is relatively small, lightweight and water resistant (see Figure 17). The unit uses a built-in lithium-ion battery that is capable of continuous operation for up to 48 hours. This GPS tracking unit has a line-of-sight range of up to 11km (Garmin 2011). The Garmin Astro handheld device was used to monitor and track up to ten DC-40 GPS units per handheld device.

Figure 17. Garmin DC-40 GPS tracking collar.

Table 2 outlines the sensor configuration, sampling frequency and observation accuracy for the two types of buoys that were deployed.

Table 2. Wave buoys with sensor configurations and accuracies.

	Datawell DWR-G4			Wave Resolving Drifter (WRD)	
	Datawell GPS	GT-31 GPS	X6-2 Accelerometer	GT-31 GPS	X6-2 Accelerometer
Sampling frequency (Hz)	1.28	1.0	10.0	1.0	10.0
Horizontal position (m)	0.01	10.0	-----	10.0	-----
Vertical elevation (m)	0.01	10.0	-----	10.0	-----
Horizontal velocity (m/s)	-----	0.1	-----	0.1	-----
Vertical velocity (m/s)	-----	0.1	-----	-----	-----
Horizontal acceleration (m/s^2)	-----	-----	0.004	-----	0.004
Vertical acceleration (m/s^2)	-----	-----	0.006	-----	0.006

B. NEARSHORE WAVE EVOLUTION

1. Experiment Location

The nearshore buoy deployments were conducted during four cruises in and around the Golden Gate channel (see Figure 18), at the entrance to San Francisco Bay, CA. The San Francisco Bay is the largest coastal bay/estuary on the west coast of the United States and is characterized by large broad shallow expanses with a relatively narrow and deep navigable channel (Conomos et al. 1985).

The Golden Gate Channel is situated at the mouth of San Francisco Bay. It is bounded by the San Francisco peninsula to the south and the Marin peninsula to the north. This channel is the only connection between San Francisco Bay and the Pacific Ocean. The width of the Golden Gate channel varies from 1.6 km to 4.0 km, with a maximum depth of 113m due to the hydrodynamic scouring from the intensified water flow through the constrictive geography.

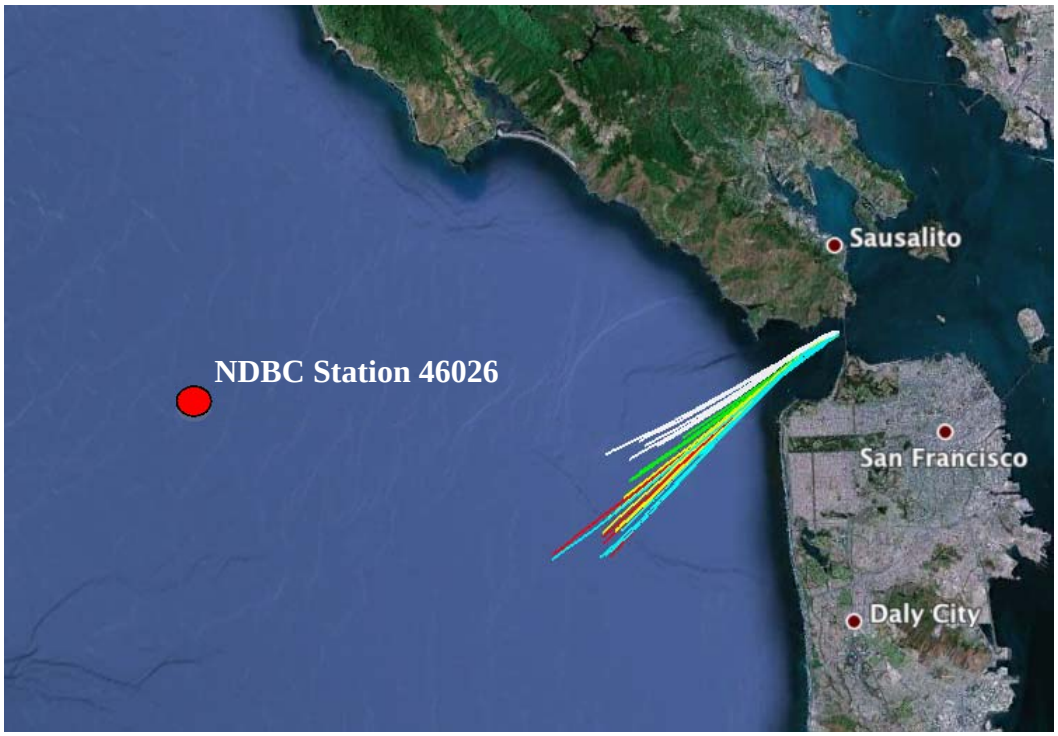

Figure 18. Location of the nearshore deployment near San Francisco, CA. Example drift tracks following the ebb current are shown. The position of NDBC Buoy 46026 is noted (From Google Earth).

The combined tidal freshwater river inflow to Suisun Bay in the northern reach of San Francisco Bay results in an "enormous tidal prism of 2 x 10^9 cubic meters (528 billion gallons)" (Barnard et al. 2006). This tidal prism produces extreme tidal currents into and out of San Francisco Bay where peak flood currents (flowing into the bay) can reach speeds of 2.5 m/s and peak ebb currents (out of the bay) can reach speeds of 3.0 m/s. This large tidal prism also results in extreme sediment transport. Sediments washed down from the Sierra Nevada Mountains through the Sacramento and San Joaquin Rivers are carried out of San Francisco Bay through the Golden Gate Channel. Outside the channel these sediments have been deposited over time resulting in a crescent-shaped ebb-tidal shoal that is only five meters deep at its shallowest location. This ebb-tidal shoal surrounds the mouth of the Golden Gate Channel and presents a significant and unique bathymetric feature that affects the approaching wave field (see Figure 19).

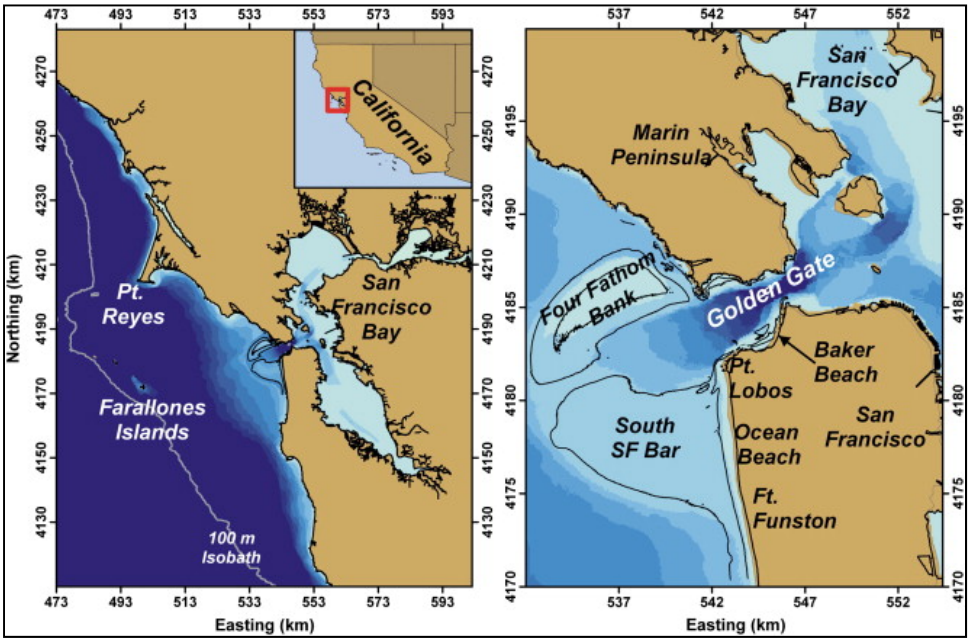

Figure 19. Ebb-tidal shoal located at the mouth of the San Francisco Bay (From Elias and Hansen 2012).

In addition to the ebb-tidal shoal, the extreme tidal currents and sediment transport through the Golden Gate Channel result in large sand waves at the mouth of the channel (see Figure 20). These sand waves have an average wavelength of 82 meters and

an average height of six meters (Barnard et al. 2006). The sand wave field at the mouth of the Bay is comprised of more than 40 individual sand waves and occurs in depths as shallow as 30 meters. Although the largest of these sand waves occur in the deeper portions of the channel and do not pose any hazard to shipping, they do influence the water depth, ultimately affecting the surface current and wave evolution.

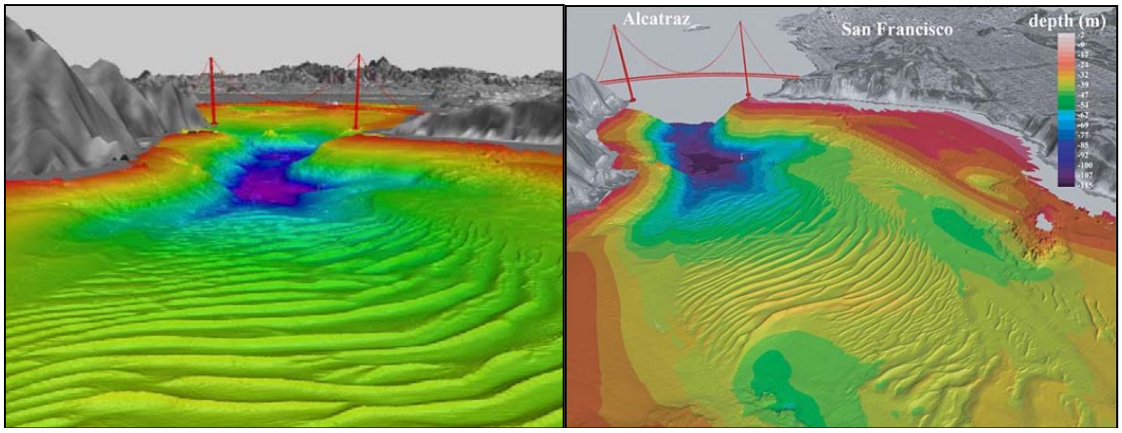

Figure 20. Sand waves located near the mouth

2. Atmospheric Conditions

NDBC Station 46026 is a 3m discus buoy maintained by the NDBC. This station provides hourly observations of atmospheric pressure, air temperature, surface wind speed (at 10m above the sea surface), surface wind direction, wave height, dominant wave period, average wave period, mean wave direction and sea surface temperature.

During the February deployment, offshore winds came out of the northwest (317°), increasing overnight on February 15th before abating late in the morning on February 16th. The surface winds peaked at 13.8m/s at 1950. The offshore wave field steadily came out of the west-northwest and varied in height between 2.14m and 3.26m. Hourly observations from station 46026 for February 15-16 are given in Table 3 and Figure 21. A peak ebb current of 4.2kts occurred in the Golden Gate channel at 1718UTC.

Table 3. Atmospheric and wave conditions reported by NDBC Buoy 46026 for February 15th-16th, 2012.

	Time (UTC)	Wind Dir	Wind Spd (m/s)	Gust (m/s)	Wave Dir	Wave Hgt (m)	Wave Per (sec)	Predicted Current (kts)
Feb 15	1350	289	7.1	8.8	284	2.75	16	Slack
	1450	268	5.7	7.4	281	2.26	14.81	Ebb
	1550	268	7.6	8.9	278	2.2	16	Ebb
	1650	312	11.8	15.4	278	2.46	14.81	Ebb
	1750	311	13.3	16.2	282	2.52	13.79	Ebb (4.2)
	1850	312	13.3	16.7	286	2.66	14.81	Ebb
	1950	317	13.8	16.8	285	2.99	16	Ebb
	2050	320	12.1	14.4	288	3.26	16	Ebb
	2150	328	11.7	14	308	3.25	7.69	Ebb
	2250	334	10.6	12.2	311	2.8	7.69	Slack
	2350	324	10.9	13.2	294	2.7	16	Flood
Feb 16	0050	326	11.2	13	296	2.38	14.81	Flood
	0150	326	10.6	12.7	281	2.37	14.81	Flood (3.0)
	0250	324	11.1	12.9	296	2.49	16	Flood
	0350	325	10.6	12.6	292	2.72	16	Flood
	0450	327	8.5	10.6	285	2.33	13.79	Slack
	0550	314	10.8	12.8	288	2.42	16	Ebb
	0650	321	10.3	12	285	2.49	14.81	Ebb (1.7)
	0750	320	10.5	12.3	262	2.14	14.81	Ebb
	0850	324	10.8	13.5	280	2.58	14.81	Ebb
	0950	319	9.6	11.9	284	2.81	14.81	Slack
	1050	336	8.1	9.5	275	2.81	14.81	Flood
	1150	333	7.2	8.9	289	2.68	14.81	Flood
	1250	318	6.1	7.5	260	2.72	14.81	Flood (2.4)
	1350	307	7.7	9.1	272	2.79	14.81	Flood
	1450	327	6	7.7	278	2.28	12.12	Flood
	1550	326	6	7.4	287	2.24	14.81	Slack
	1650	321	8.5	9.9	284	2.15	13.79	Ebb
	1750	325	8.2	9.7	283	2.18	13.79	Ebb

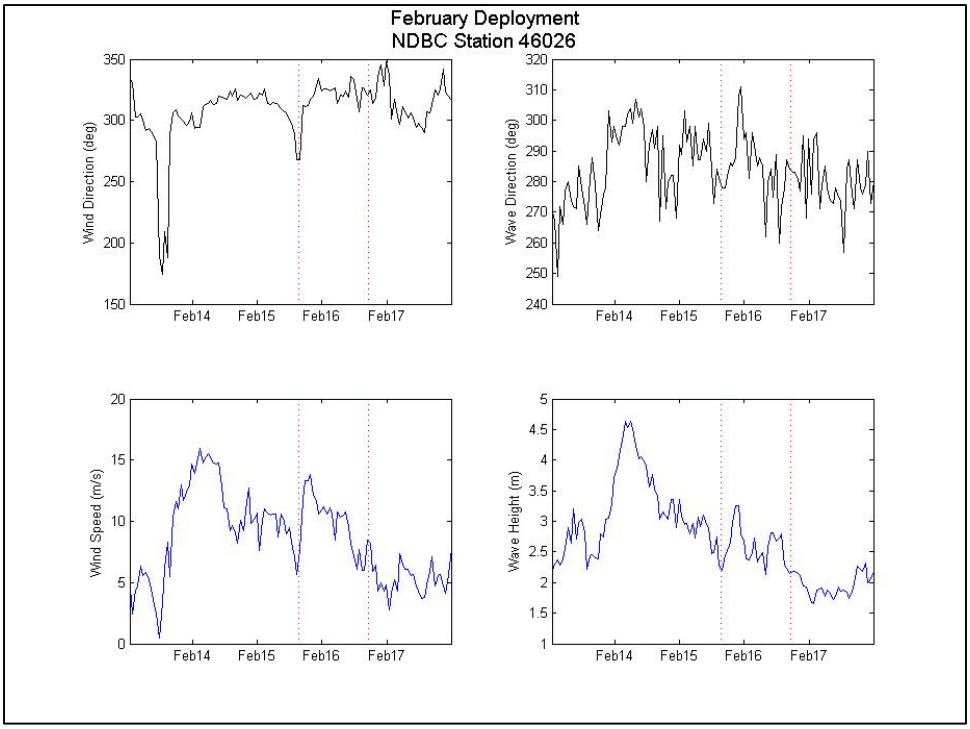

Figure 21. Wind speed and offshore wave height recorded at NDBC Station 46026 for the February deployment.

During the April deployment, offshore winds were relatively consistent coming out of the northwest at 10m/s. The offshore wave field steadily came out of the west-northwest and slowly increased in height during the deployment to a significant wave height of 2.56m. Hourly observations from station 46026 on April 27 are given in Table 4 and Figure 22. A peak ebb current of 3.5kts occurred in the Golden Gate channel at 1558UTC.

Table 4. Atmospheric and wave conditions reported by NDBC Buoy 46026 for April 27th, 2012.

	Time (UTC)	Wind Dir	Wind Spd (m/s)	Gust (m/s)	Wave Dir	Wave Hgt (m)	Wave Per (sec)	Predicted Current (kts)
Apr 27	0050	292	9.2	10.7	268	1.06	16	Flood
	0150	295	7.8	9.3	247	1.35	14.81	Slack
	0250	293	6.2	7.3	297	1.32	10	Ebb
	0350	296	7.4	8.8	294	1.37	9.09	Ebb (1.6)
	0450	295	6.3	7.7	303	1.5	9.09	Ebb
	0550	298	6.1	7.4	288	1.65	9.09	Ebb
	0650	300	6	7.6	284	1.66	10.81	Slack
	0750	299	5.4	6.7	290	1.63	8.33	Flood
	0850	296	5	6.5	289	1.64	10	Flood
	0950	298	6.9	7.9	283	1.66	10	Flood (1.5)
	1050	295	7.9	9.5	293	1.58	10	Flood
	1150	299	8.3	9.5	294	1.54	10	Flood
	1250	305	9.5	11.3	249	1.71	13.79	Slack
	1350	313	8.5	10.1	299	1.95	10	Ebb
	1450	310	9	10.5	295	1.83	9.09	Ebb
	1550	315	9.5	11.5	300	2.09	10	Ebb (3.5)
	1650	316	9.9	11.9	302	2.07	10	Ebb
	1750	316	10.6	12.3	304	2.16	10	Ebb
	1850	310	10.8	12.9	291	2.19	10	Ebb
	1950	314	11.1	12.8	297	2.2	10.81	Slack
	2050	314	10.3	12.3	300	2.28	10.81	Flood
	2150	317	10.4	12.3	297	2.56	12.12	Flood
	2250	320	10.4	12.2	279	2.27	13.79	Flood (2.5)
	2350	317	10.5	12.4	298	2.4	12.12	Flood

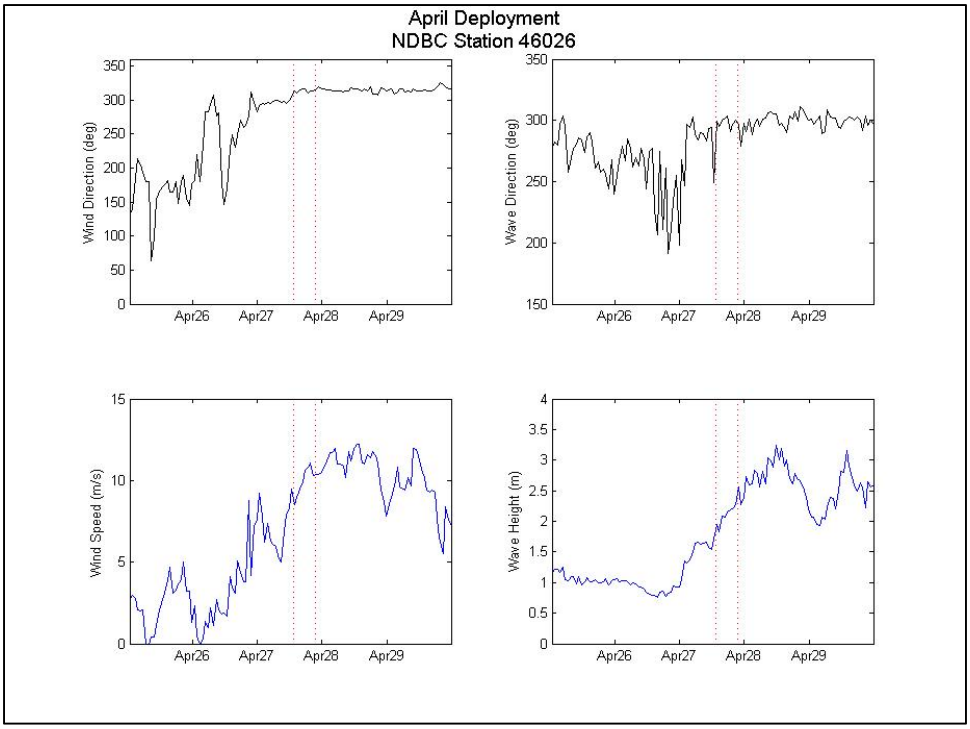

Figure 22. Wind speed and offshore wave height recorded at NDBC Station 46026 for the April deployment.

3. Buoy Deployment

On February 15th, 2012, 20 WRD buoys were deployed from R/V Questuary underneath the Golden Gate Bridge. The buoys were deployed individually at approximately 12 minute intervals. The buoys drifted out the channel on the outgoing ebb tide where they were later recovered at various times by R/V Point Sur. Some of the buoys remained adrift for more than 24 hours. Seven of the buoys were ultimately lost and/or damaged after washing ashore north and south of the channel. This deployment captured the broad circulation characteristics of the tidal inlet.

On April 27th, 30 WRD buoys were deployed from R/V Questuary in the center of the ebb-tidal jet (as determined by ADCP transects), underneath the Golden Gate Bridge. The buoys were deployed in groups of five. There was a one minute interval between buoys and five minute intervals between groups. The buoys were deployed on an increasing ebb-tidal current and drifted out the Golden Gate. The buoys were recovered by R/V Point Sur after they had drifted seaward of the San Francisco bar (ebb-tidal shoal).

THIS PAGE INTENTIONALLY LEFT BLANK

III. DATA PROCESSING AND ANALYSIS

A. DATA CONSOLIDATION

1. Data Extraction

The raw data was extracted from the DWR-G buoy and WRD sensors in order to create one consolidated data structure for analysis and comparison (see Table 5). The DWR-G buoy recorded raw horizontal and vertical displacements in a proprietary Datawell binary format. In addition, it recorded the internally processed wave height and directional spectra that were not used in this study. The raw data extracted from the DWR-G provided four data strings: GPS time, easting displacement, northing displacement and vertical displacement. These data strings were all sampled at 1.28Hz. A 30 second moving average was removed from the three displacement data strings in order to remove any low-frequency signal (Herbers et al. 2012).

The GT-31 GPS receiver recorded the GPS time, latitude, longitude, positional displacements and horizontal Doppler velocities on an internal SD card. The data extracted from the GT-31 provided six data strings: GPS time, easting displacement, northing displacement, vertical displacement, easting Doppler velocity and northing Doppler velocity. All of these data strings were sampled at 1Hz. Similar to the DWR-G time series, a 30 second moving average was removed from the displacement data strings in order to remove any low-frequency trend or signal (Herbers et al. 2012). All of the DWR-G and GT-31 data stings were linearly interpolated to 10Hz in order to match the sampling frequency of the accelerometer.

The first step of the consolidation aligned all of the raw data strings on a synchronized time base. Since the DWR-G displacements were achieved through an integration of the observed GPS signal Doppler shift, the DWR-G time was internally interpolated between the buoy's 30-minute GPS fixes (Datawell 2010). Therefore, the more accurate GT-31 GPS time was used as the absolute time. A cross correlation

analysis between the easting displacements of the GT-31 and the DWR-G provided the timing adjustment required to align the DWR-G displacements in accordance with the GT-31 time (Herbers et al. 2012).

The data extracted from the X6–2 accelerometer provided three data records: acceleration in the x-axis direction, acceleration in the y-axis direction and acceleration in the z-axis direction). The vertically oriented axis of the accelerometer was easily identified based on the large gravitational signal. The vertical acceleration string was integrated once in order to calculate the vertical velocity, and similar to the GPS time series, a 30 second moving average was removed in order to remove any low-frequency noise. These velocity data were then linearly interpolated to 10Hz. Next, a cross correlation analysis between the vertical velocities of the X6–2 and the easting and northing displacements of the GT-31 provided the timing adjustment required to align the X6–2 velocities in accordance with the GT-31 time. The vertical velocity string was then integrated once more (again removing a 30 second moving average) in order to calculate the vertical displacement. A final cross-correlation analysis between the vertical displacements of the X6–2 and the vertical displacements of the DWR-G verified that the X6–2 displacements where aligned in accordance with the GT-31 time.

Finally, the synchronized data strings from the sensors were consolidated into one data structure which contained: GPS time, GPS latitude, GPS longitude, DWR-G easting displacement, DWR-G northing displacement, DWR-G vertical displacement, GT-31 easting displacement, GT-31 northing displacement, GT-31 vertical displacement, GT-31 easting velocity, GT-31 northing velocity, X6–2 vertical acceleration, X6–2 vertical velocity and X6–2 vertical displacement. All data strings were now sampled at 10Hz and aligned on the GT-31 GPS time (see Table 5). This process allowed for the direct comparison of the time series from the various sensors.

Table 5. Raw and consolidated data output from the various buoy sensors.

Data string	Raw variable		Final structure	
	Sample rate	Time source	Sample rate	Time source
GT-31 time (UTC)	1.0	GT-31	10.0	GT-31
GT-31 latitude	1.0	GT-31	10.0	GT-31
GT-31 longitude	1.0	GT-31	10.0	GT-31
Datawell time (UTC)	1.28	Datawell	10.0	GT-31
Datawell easting displacement	1.28	Datawell	10.0	GT-31
Datawell northing displacement	1.28	Datawell	10.0	GT-31
Datawell vertical displacement	1.28	Datawell	10.0	GT-31
GT-31 easting displacement	1.0	GT-31	10.0	GT-31
GT-31 northing displacement	1.0	GT-31	10.0	GT-31
GT-31 vertical displacement	1.0	GT-31	10.0	GT-31
GT-31 easting Doppler velocity	1.0	GT-31	10.0	GT-31
GT-31 northing Doppler velocity	1.0	GT-31	10.0	GT-31
X6-2 easting acceleration	10.0	X6-2	10.0	GT-31
X6-2 northing acceleration	10.0	X6-2	10.0	GT-31
X6-2 vertical acceleration	10.0	X6-2	10.0	GT-31
X6-2 vertical velocity	-----	-----	10.0	GT-31
X6-2 vertical displacement	-----	-----	10.0	GT-31

2. Time Series Characteristics

The consolidated time series of the validation dataset included 307,199 data points, corresponding to 8.53 hours of data. The nearshore datasets varied in length from 1.25 hours to 25.38 hours of data depending on the buoy deployment. The Nyquist frequency of the buoy's sensors $\left(f_N = \frac{1}{2\Delta t} \right)$ determines the maximum frequency that can be used in the spectral analysis. The Nyquist frequency of the Datawell buoy is 0.64Hz, while the Nyquist frequency of the GT-31 GPS receiver and the X6–2 accelerometer are 0.50Hz and 5Hz, respectively. So, the DWR-G is capable of resolving waves with a period as short as 1.56 seconds, while the WRD buoy is capable of resolving waves with a period as short as 2 seconds. The interpolation of the data strings to 10Hz was performed on the collected data, thus it does not affect the sensor's Nyquist frequency, and does not increase the buoy's ability to resolve shorter period waves.

3. Linear Wave Theory Transfer Functions

The present dataset provides robust measurements of various properties of the wave orbital motion. Through the application of linear wave theory, these measurements can be used to estimate wave frequency and direction spectra, as well as bulk wave statistics (Herbers et al. 2012).

Assuming that the wave height is sufficiently smaller than the wavelength and that the current speed (buoy drift rate) is sufficiently smaller than the wave propagation speed, linear wave theory relates the orbital motion of the water particles to the sea surface elevation (wave height) (Herbers et al. 2012). To derive these transfer functions, the surface elevation (η) is expressed as a sum of Fourier components with different frequencies (ω) and propagation directions

$$\eta(x,t) = \sum_{\omega}\sum_{\theta} A_{\omega\theta} \exp\left[i\left(\vec{k}\cdot\vec{x} - \omega t\right)\right] + c.c., \tag{2}$$

where $\vec{k}$ is the wave-number vector and c.c. is the complex conjugate. The wave number magnitude $k = \left|\vec{k}\right|$ is related to ω through the linear dispersion relation (Equation 1).

Transfer functions are first derived in order to relate the vertical motion (velocity and acceleration) to the surface height (η) at a fixed location $(\vec{x} = 0)$, neglecting the drift of the buoy. The vertical velocity *w(t)* follows from taking the first time-derivative of η at $\vec{x} = 0$. Similarly, the vertical acceleration *a(t)* equals the second derivative of the sea surface displacement equation.

$$w(t) = \sum_{\omega}\sum_{\theta} -i\omega A_{\omega\theta} \exp\left(-i\omega t\right) + c.c. \tag{3}$$

$$a(t) = \sum_{\omega}\sum_{\theta} -\omega^2 A_{\omega\theta} \exp\left(-i\omega t\right) + c.c. \tag{4}$$

Next, transfer functions are derived in order to relate the horizontal motion (velocity and displacement) to the surface elevations (vertical displacement). The momentum equations relate the horizontal accelerations to the slopes of the sea surface:

$$\frac{du}{dt} = -g\frac{\partial \eta}{\partial x} \tag{5}$$

$$\frac{dv}{dt} = -g\frac{\partial \eta}{\partial y} \tag{6}$$

.

Differentiating the sea surface displacement with respect to $\vec{x}$ and integrating with respect to t (at $\vec{x} = 0$) yields the horizontal velocities *(u, v)*:

$$u(t) = \sum_{\omega}\sum_{\theta}\frac{gk}{\omega}\cos\theta A_{\omega\theta}\exp(-i\omega t) + c.c. \tag{7}$$

$$v(t) = \sum_{\omega}\sum_{\theta}\frac{gk}{\omega}\sin\theta A_{\omega\theta}\exp(-i\omega t) + c.c. \tag{8}$$

Finally, the horizontal displacements *(x, y)* are derived from integrating the horizontal velocities (Equations 7 and 8) with respect to *t* once more,

$$x(t) = \sum_{\omega}\sum_{\theta}\frac{igk}{\omega^2}\cos\theta A_{\omega\theta}\exp(-i\omega t) + c.c. \tag{9}$$

$$y(t) = \sum_{\omega}\sum_{\theta}\frac{igk}{\omega^2}\sin\theta A_{\omega\theta}\exp(-i\omega t) + c.c. \tag{10}$$

The frequency-dependent coefficients of the transfer functions are summarized in Table 6.

Table 6. Derived coefficients for the transfer functions used to relate measured surface motion to sea surface displacement.

		Vertical displacement
Measured surface motion	Horizontal displacement	$\frac{igk}{\omega^2}$
	Horizontal velocity	$\frac{gk}{\omega}$
	Vertical acceleration	$-\omega^2$

B. SPECTRAL ANALYSIS TECHNIQUES

The time series of wave-induced surface motions can be analyzed spectrally through the use of the Fast Fourier Transform (FFT), which relates the time-dependent motions to the wave energy spectrum (*E(f)*). This analysis provides an assessment of how the wave energy is distributed across a specific frequency band. For example, a spectral peak can identify a dominant wave period of a dataset. A cross-spectral analysis was performed using various combinations of the horizontal and vertical motion time series to estimate the mean wave direction, $\overline{\theta}(f)$ and the directional spread, $\sigma_\theta(f)$ as a function of frequency. Finally, the bulk wave statistics (significant wave height, mean wave period, mean wave direction and directional spreading) were estimated from the frequency and direction spectra.

Bulk values of $\overline{\theta}$ and σ_θ are estimated by replacing the auto- and cross-spectra in Table 7 with the integrals over the same frequency range $f_1 - f_2$. The auto-spectra, $E_{xx}(f)$, $E_{yy}(f)$, $E_{zz}(f)$, and cross-spectra, $C_{xy}(f)$, $C_{xz}(f)$, $C_{yz}(f)$, for each surface motion time series were calculated utilizing the Matlab cross power spectral density function (CPSD). The CPSD function utilizes a specified FFT record length with a 50% overlap of samples. The resultant spectrum was then merged across a number of frequency bands. Next, following Herbers et al. (2012), the frequency was restricted to 0.05Hz – 0.3Hz in order to only examine the swell-sea frequency range (wave periods 3.3 – 20 seconds).

1. Directional Estimates

The directional Fourier coefficients (see Long, 1980 for definitions) were estimated from the auto- and cross-spectra using the relations in Table 7 which incorporate the transfer functions of Table 6 for the various measurement combinations. The first-order coefficients a_1, b_1 depend on both vertical and horizontal wave-induced surface motions; the second-order coefficients a_2, b_2 depend only on horizontal motions (and thus are not affected by errors in the acceleration measurements, see e.g. Herbers et al. 2012).

Table 7. Estimates of the directional Fourier coefficients for different combinations of measurements.

	x, y, z	x, y, a	u, v, a
a_1	$\frac{C_{xz}}{\sqrt{E_{zz}\left(E_{xx}+E_{yy}\right)}}$	$\frac{-C_{xa}}{\sqrt{E_{aa}\left(E_{xx}+E_{yy}\right)}}$	$\frac{Q_{ua}}{\sqrt{E_{aa}\left(E_{uu}+E_{vv}\right)}}$
b_1	$\frac{C_{yz}}{\sqrt{E_{zz}\left(E_{xx}+E_{yy}\right)}}$	$-\frac{C_{ya}}{\sqrt{E_{aa}\left(E_{xx}+E_{yy}\right)}}$	$\frac{Q_{va}}{\sqrt{E_{aa}\left(E_{uu}+E_{vv}\right)}}$
a_2	$\frac{\left(E_{xx}-E_{yy}\right)}{\left(E_{xx}+E_{yy}\right)}$	$\frac{\left(E_{xx}-E_{yy}\right)}{\left(E_{xx}+E_{yy}\right)}$	$\frac{\left(E_{uu}-E_{vv}\right)}{\left(E_{uu}+E_{vv}\right)}$
b_2	$\frac{2C_{xy}}{\left(E_{xx}+E_{yy}\right)}$	$\frac{2C_{xy}}{\left(E_{xx}+E_{yy}\right)}$	$\frac{2C_{uv}}{\left(E_{uu}+E_{vv}\right)}$

The mean wave direction ($\bar{\theta}$) and directional spread (σ_θ) were estimated from both the first- and second-order Fourier moments (a_1, b_1) (Herbers et al. 2012, Kuik 1988). The first-order estimates, given by

$$\tan\left(\bar{\theta}\right)=\frac{b_1}{a_1} \tag{11}$$

$$\sigma_\theta=\sqrt{2\left(1-\sqrt{a_1^2+b_1^2}\right)} \tag{12}$$

are widely used in routine analysis of wave buoy observations.

The second-order estimates

$$\tan\left(2\bar{\theta}\right)=\frac{b_2}{a_2} \tag{13}$$

$$\sigma_\theta=\sqrt{\frac{\left(1-\sqrt{a_2^2+b_2^2}\right)}{2}} \tag{14}$$

suffer from a 180 ambiguity, but do not rely on vertical surface motions, and thus provide a useful consistency check on the quality of the directional wave data (Herbers et al. 2012).

2. Wave Parameters

The significant wave height and wave period are readily estimated from the wave energy spectrum (Herbers et al. 2012). The significant wave height is commonly defined as the average of the largest one third of the waves. Spectrally, this is equivalent to four times the variance of the wave energy spectrum.

$$H_S = 4\sqrt{\int_{f_1}^{f_2} E(f)\,df} \tag{15}$$

where f_1 and f_2 specify the frequency range of interest.

The mean wave period was estimated spectrally from the frequency-weighted mean of the wave energy spectrum.

$$T_m = \frac{\int_{f_1}^{f_2} E(f)\,df}{\int_{f_1}^{f_2} f \cdot E(f)\,df} \tag{16}$$

3. Wave Motion Analysis

As noted before, wave frequency and direction spectra (and associated bulk statistics) were calculated using various combinations of time series of horizontal and vertical motions to compare the calculated statistics from different buoy sensors. The first processed method utilized both the horizontal and vertical DGPS displacements (x,y,z). This method was used for analyzing the DWR-G and some of the GT-31 data. The second processing method utilized horizontal DGPS displacements from the GT-31 (x,y) and vertical accelerations from the X6–2 (a). Finally, the third processing method utilized horizontal Doppler velocities from the GT-31 (u,v) and vertical accelerations from the X6–2 (a).

IV. WAVE RESOLVING DRIFTER VALIDATION

The validation of the WRD buoy focused on evaluating the sensor accuracy and buoy response in energetic open ocean wave conditions using the well tested Datawell DWR-G buoy as a "ground truth." The first step of the validation was a comparison of measurements from WRD sensors (GT-31 GPS receiver and X6–2 accelerometer) collocated on a DWR-G buoy with the DWR-G measurements. The second step of the validation was an evaluation of the overall performance of the buoy design by comparing the measurements from the three WRD buoys with measurements from the DWR-G buoy, all drifting in close proximity to each other.

A. SPECTRAL PROCESSING

Prior to conducting the comparisons, the time series were analyzed in order to determine the optimal processing parameters. An analysis of various FFT record lengths and merging of frequency bands was done. The results of these analyses were used to process all of the spectra and statistics.

1. FFT Record Length

Various FFT record lengths were analyzed to determine the optimal frequency resolution while still resolving the temporal variations in wave conditions. These record lengths included 1024 data points (1.7 minutes of data), 2048 data points (3.4 minutes of data), 4096 data points (6.8 minutes of data), 8192 data points (13.7 minutes of data) and 16384 data points (27.7 minutes of data).

A comparison of the statistics calculated from the DWR-G displacement data (see Table 8) showed that the bulk wave statistics calculated from FFT record lengths of 16384 samples and 8192 samples agreed well with the statistics calculated from the entire time series. All of the bulk wave statistics (calculated from both horizontal and vertical motions) differed by less than 1% and less than 2.5% respectively. Specifically, the significant wave heights differed by less than 0.02m for an FFT record length of 16384 samples and differed by less than 0.09m for a record length of 8192 samples. The mean

wave direction and directional spread differed by less than 1° for both of these record lengths.

The statistics calculated from the other FFT record lengths (4096, 2048 and 1024) also agreed well, differing by less than 8.5% when compared to the entire time series. Of note, the significant wave heights differed by less than 6.5% (0.21m) for an FFT record length of 4096 samples. These statistics improved slightly for an FFT record length of 2048 samples, differing by less than 3.5% (0.09m). The mean wave direction differed by less than 1° for these record lengths while the directional spread differed by less than 2.5°. The mean wave period was within 4.5% (0.37sec) for these record lengths.

Table 8. Bulk wave statistics for various FFT record lengths compared to the statistics calculated from the entire time series using the Datawell DGPS displacement data.

Datawell GPS Displacements											
Vertical Orbital Motions	**Total**	**FFT: 1024**	**Diff**	**FFT: 2048**	**Diff**	**FFT: 4096**	**Diff**	**FFT: 8192**	**Diff**	**FFT: 16384**	**Diff**
Significant wave height (m)	3.31	3.38	2.37 %	3.38	2.21 %	3.48	5.16 %	3.37	1.85 %	3.31	-0.02 %
Mean wave period (sec)	8.17	8.28	1.33 %	8.25	1.05 %	8.36	2.35 %	8.25	1.04 %	8.18	0.09 %
Mean wave direction (deg)	309.94	310.33	0.39°	310.36	0.42°	309.32	-0.62°	309.04	-0.90°	309.64	-0.30°
Directional spread (deg)	26.99	26.90	-0.09°	24.76	-2.23°	25.77	-1.22°	26.91	-0.08°	27.09	0.10°
Horizontal Orbital Motions	**Total**	**FFT: 1024**	**Diff**	**FFT: 2048**	**Diff**	**FFT: 4096**	**Diff**	**FFT: 8192**	**Diff**	**FFT: 16384**	**Diff**
Significant wave height (m)	3.38	3.58	5.73 %	3.48	3.02 %	3.58	6.01 %	3.43	1.54 %	3.39	0.35 %
Mean wave period (sec)	8.32	8.66	4.08 %	8.35	0.36 %	8.58	3.13 %	8.41	1.09 %	8.34	0.30 %
Mean wave direction (deg)	311.48	311.71	0.23°	311.37	-0.11°	310.44	-1.04°	310.38	-1.10°	310.97	-0.51°
Directional spread (deg)	20.65	20.16	-0.49°	19.57	-1.08°	19.73	-0.92°	20.66	0.01°	20.77	0.12°

Scatter plots comparing the statistics of the DWR-G displacements and various FFT record lengths are shown in Figure 22 with statistics from vertical displacements plotted as squares and statistics from horizontal displacements plotted as circles. The plots show excellent agreement for all of the FFT record lengths except for a record length of 1024 samples. The best agreement is seen using record lengths of 16834 and 8192 samples.

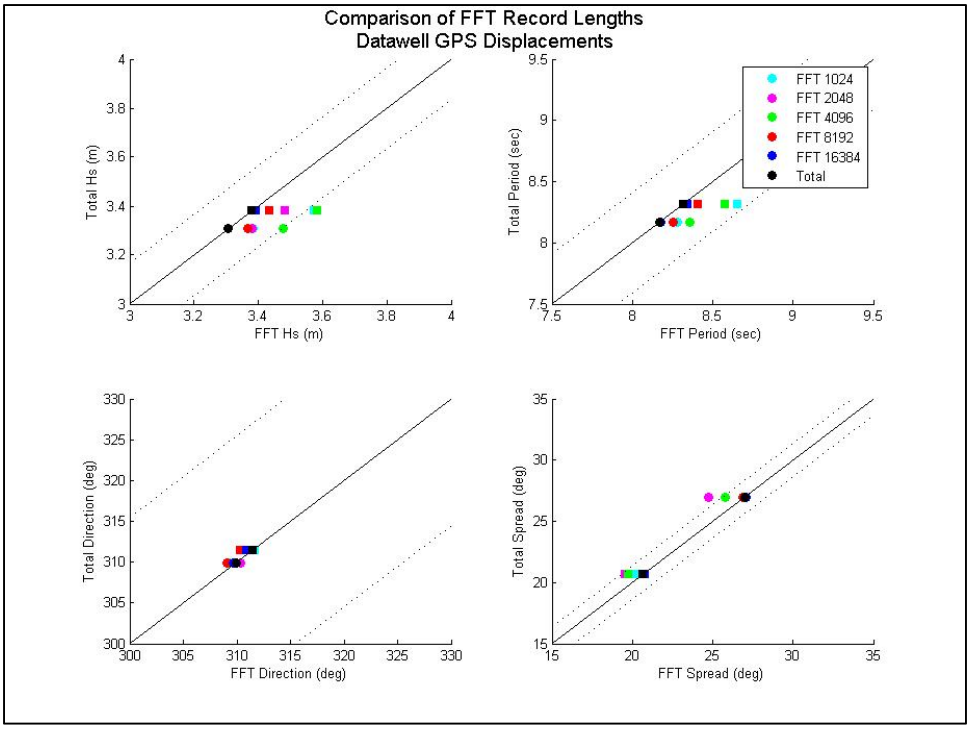

Figure 23. Scatter plot comparison of the bulk wave statistics using various FFT record lengths of DWR-G DGPS displacements compared to statistics using the entire time series. Statistics calculated from vertical displacements are plotted as circles, while statistics calculated from horizontal displacements are plotted as squares. The top left panel is significant wave height, the top right panel is mean wave period, the bottom left panel is mean wave direction and the bottom right panel is directional spread. The dashed lines represent +/- 5% from the statistic of the entire time series.

A comparison of estimates based on GT-31 DGPS displacements versus GT-31 Doppler velocities also showed excellent agreement for record lengths of 16384 and 8192 samples with differences within 1.5% and 2.5% respectively (see Table 9). Statistics calculated from shorter record lengths of 4096 and 2048 were somewhat degraded (errors within 10%) with larger errors for a record length of 1024 samples.

Table 9. Bulk wave statistics calculated for various FFT record lengths compared to the statistics calculated from the entire time series using various configurations of the GT-31 DGPS displacements, GT-31 Doppler velocity and X6-2 acceleration data.

Datawell GT-31 DGPS Displacements			
Vertical Orbital Motions	**Total**	**FFT: 8192**	**Diff**
Significant wave height (m)	1.75	1.87	6.98 %
Mean wave period (sec)	9.1	9.1	0.01 %
Mean wave direction (deg)	309	308	-0.95°
Directional spread (deg)	41	41	-0.11°
Horizontal Orbital Motions	**Total**	**FFT: 8192**	**Diff**
Significant wave height (m)	3.31	3.39	2.35 %
Mean wave period (sec)	8.8	8.9	1.97 %
Mean wave direction (deg)	311	310	-0.34°
Directional spread (deg)	22	22	0.16°
Datawell GT-31 DGPS Displacements and X6-2 Accelerations			
Vertical Orbital Motions	**Total**	**FFT: 8192**	**Diff**
Significant wave height (m)	3.50	3.56	1.57 %
Mean wave period (sec)	8.0	8.1	0.60 %
Mean wave direction (deg)	309	309	-0.53°
Directional spread (deg)	34	35	1.21°
Horizontal Orbital Motions	**Total**	**FFT: 8192**	**Diff**
Significant wave height (m)	3.31	3.39	2.35 %
Mean wave period (sec)	8.8	8.9	1.97 %
Mean wave direction (deg)	311	310	-0.34°
Directional spread (deg)	22	22	0.16°
Datawell GT-31 Doppler Velocities and X6-2 Accelerations			
Vertical Orbital Motions	**Total**	**FFT: 8192**	**Diff**
Significant wave height (m)	3.50	3.56	1.57 %
Mean wave period (sec)	8.0	8.1	0.60 %
Mean wave direction (deg)	309	309	-0.24°
Directional spread (deg)	34	34	0.82°
Horizontal Orbital Displacements	**Total**	**FFT: 8192**	**Diff**
Significant wave height (m)	3.50	3.57	2.15 %
Mean wave period (sec)	8.5	8.7	1.88 %
Mean wave direction (deg)	310	310	0.11°
Directional spread (deg)	22	22	0.06°

In addition to the bulk wave statistics, the wave frequency spectra were calculated estimated from the DWR-G displacement data were compared for different choices of the FFT record length (see Figure 24). As expected, these results show the trade-off between degraded resolution for short FFT record lengths versus statistical scatter for long FFT lengths. FFT record lengths of 16384 and 8192 samples appear to resolve similar spectral features across the entire frequency range, as is the case for an FFT record length of 4096 samples for most frequencies (greater than 0.08Hz). Spectra from record lengths of 2048 and 1024 samples show degraded frequency resolution at frequencies below 0.2Hz.

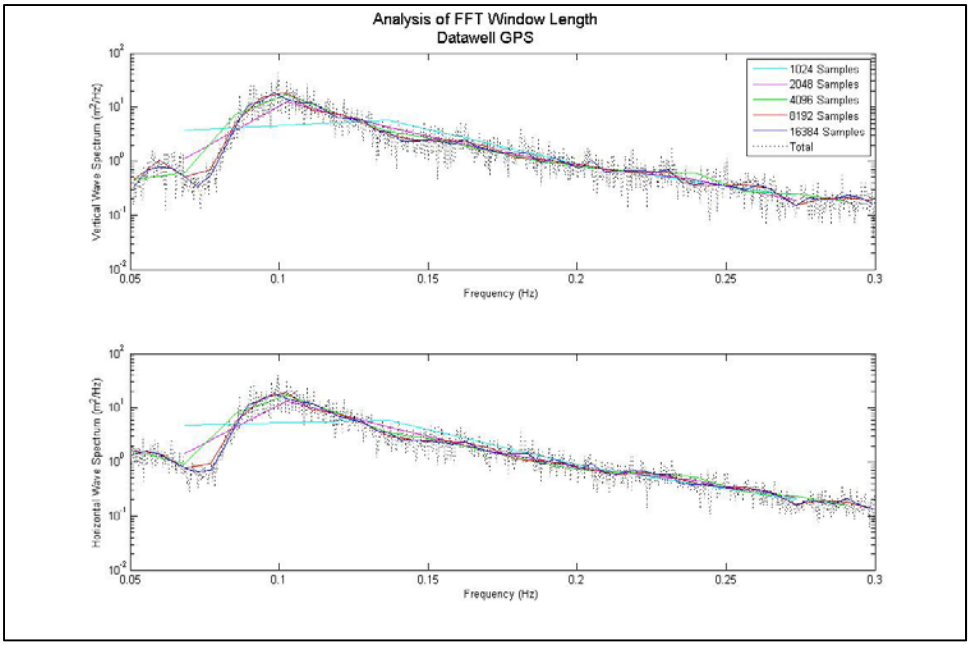

Figure 24. Wave frequency spectra calculated from various FFT record lengths of the DWR-G time series. The top panel uses vertical displacements. The bottom panel uses horizontal displacements.

2. Frequency Band Merging

Similar to the FFT record length analysis, various numbers of frequency bands (3, 5, 7 and 9) were merged together during the calculation of the wave frequency spectrum. This was done in order to smooth out the spectrum and identify spectral peaks of the swell-sea and wind-sea bands. However, as discussed in Section 3.A.2, merging frequency bands together decreases the frequency resolution. Figure 25 shows the wave frequency spectra calculated using DWR-G displacements and an FFT record length of 8192 samples. The minimum number of frequency bands merged together was three. This spectrum has the highest frequency resolution, but is difficult to accurately identify spectral peaks due to the increased number and variability of data points. Merging more frequency bands together resulted in a smoother spectral curve making the identification of spectral peaks more obvious. The optimal results are observed through the merging of seven frequency bands. This provides the best frequency resolution with the clear identification of the spectral peaks.

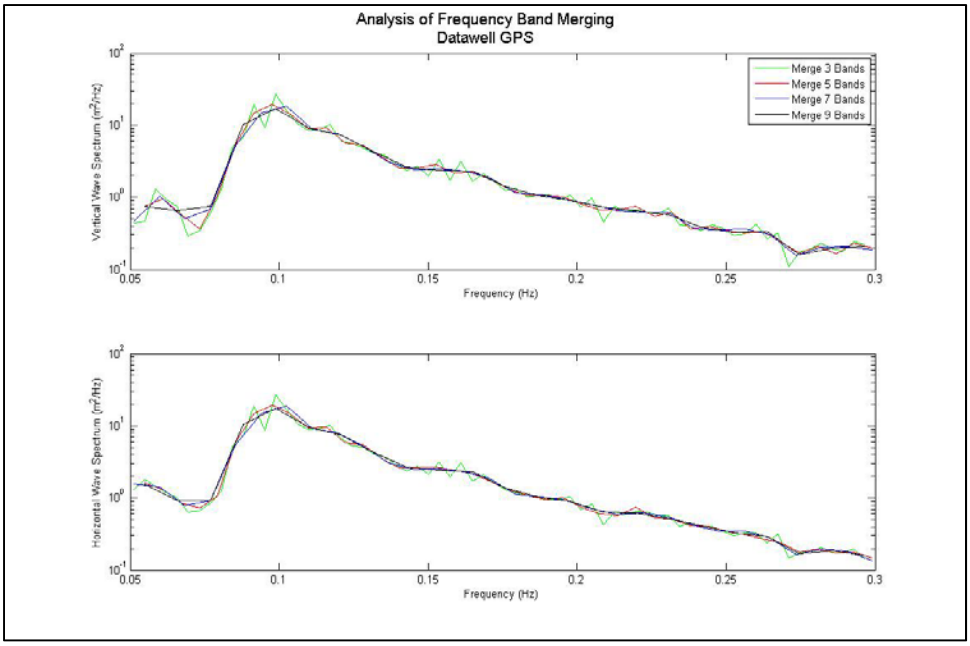

Figure 25. Wave energy spectra calculated from the DWR-G time series using an FFT record length of 8192 samples and merging various number of frequency bands. The top panel uses horizontal displacements. The bottom panel uses vertical displacements.

B. SENSOR COMPARISONS

1. Linear Interpolation of Raw Data

The various sensors all had different sampling frequencies, which were linearly interpolated to 10Hz to create the consolidated dataset. Statistical and spectral analysis was performed comparing the interpolation of the DWR-G data from 1.28Hz to 10Hz and the interpolation of the GT-31 GPS time series from 1.0Hz to 10.0Hz.

Bulk wave statistics were calculated for each time series based on both vertical and horizontal displacements. These statistics are listed in Table 10. The interpolation of the DWR-G time series introduced less than 2% error into the calculated statistics. The significant wave height differed by less than 1% (0.02m) from the original statistics. The mean wave direction and directional spread also differed by less than 1% (1.2°) from the original statistics. The largest error introduced by the interpolation was observed in the

calculation of the mean wave period; however, it was still within 2% (0.2sec) of the original statistics. There was not any significant difference between the vertical and horizontal displacements.

The interpolation of the GT-31 time series introduced slightly larger errors, but were still within 5% of the original statistics overall. The significant wave height differed by less than 2% (0.14m) from the original statistics. The mean wave direction and directional spread differed by less than 3% (approximately 1.5°) from the original statistics. Similar to the DWR-G, the largest error introduced by the interpolation was observed in the mean wave period, which differed by 5% (0.4sec) from the original statistics. Overall, there was slightly better agreement from the statistics calculated from the horizontal displacements than those calculated by the vertical displacements, which was likely caused by the decreased vertical resolution of the GT-31 GPS receiver.

Table 10. Bulk wave statistics calculated before and after the linear interpolation of the Datawell DGPS and GT-31 time series.

Linear Interpolation Comparison						
Vertical Orbital Motions	Datawell GPS			Datawell GT-31		
Sampling frequency (Hz)	1.26	10.0	Diff	1.00	10.0	Diff
Significant wave height (m)	3.38	3.37	-0.46 %	1.91	1.87	-1.70 %
Mean wave period (sec)	8.1	8.3	1.93 %	8.6	9.1	5.08 %
Mean wave direction (deg)	310	309	-1.26°	309	308	-1.42°
Directional spread (deg)	27	27	-0.17°	39	41	1.16°
Horizontal Orbital Motions	Datawell GPS			Datawell GT-31		
Sampling frequency (Hz)	1.26	10.0	Diff	1.00	10.0	Diff
Significant wave height (m)	3.45	3.43	-0.57 %	3.43	3.39	-1.06 %
Mean wave period (sec)	8.2	8.4	1.99 %	8.5	8.9	4.84 %
Mean wave direction (deg)	312	310	-1.21°	311	310	-0.77°
Directional spread (deg)	21	21	-0.26°	22	22	0.05°

Similar to the statistical comparison, a spectral analysis was performed comparing the wave frequency spectrum from the original and interpolated time series of both sensors. The spectral comparison of the DWR-G time series is shown in the top half of Figure 26. The interpolated spectrum agrees extremely well with the original spectrum identifying similar spectral peaks and spectral energy levels. The spectral comparison of the GT-31 time series is shown in the bottom half of Figure 25. Again, the interpolated

spectrum agrees very well with the original spectrum. The two spectra identify similar spectral peaks and spectral energy for frequencies less than 0.17Hz. For frequencies greater than 0.17Hz, the interpolated spectrum shows similar spectral characteristics; however, the spectral energy levels are slightly decreased due to the dilution of high frequency energy caused by the energy leakage beyond the original Nyquist frequency introduced by the linear interpolation (Pearman et al. 2013).

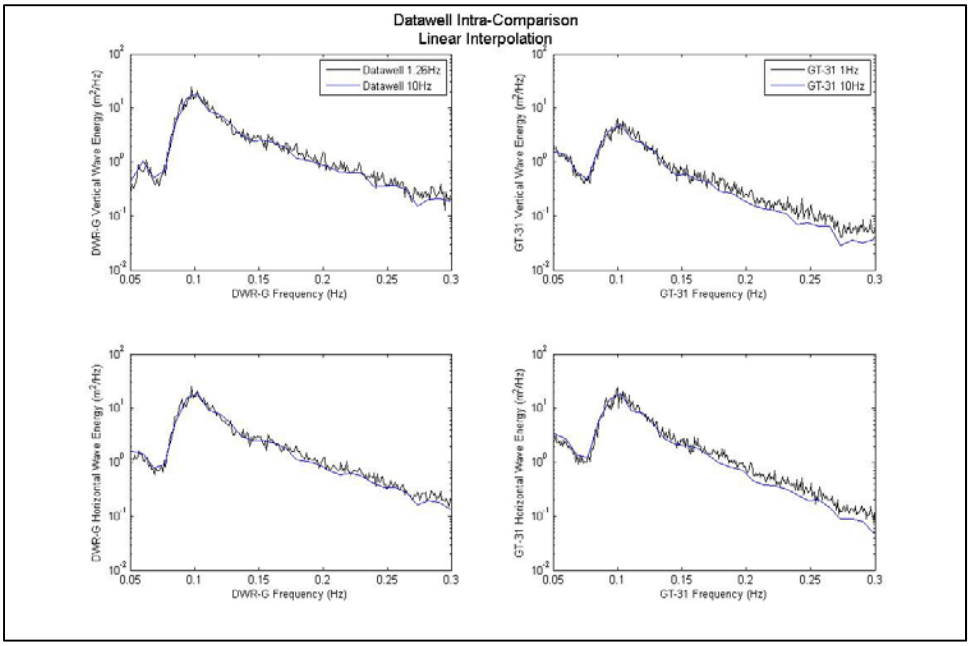

Figure 26. Spectral comparison of the linear interpolation of the time series. The left panels are the DWR-G wave spectra from vertical and horizontal displacements. The right panels are the GT-31 wave spectra from vertical and horizontal displacements.

Overall, this analysis shows that the linear interpolation of the original time series does not significantly affect the bulk wave statistics or the wave energy spectrum, particularly in the swell-sea frequency band. The linear interpolation of the GT-31 seems to slightly degrade wave energy at higher frequencies, corresponding to waves with periods shorter than five seconds which is approaching one half of the sensor's actual Nyquist frequency.

2. Horizontal Wave Motion

The GT-31 GPS receiver provided two different techniques for measuring the horizontal surface motions: traditional DGPS positioning and Doppler velocity measurements. The quality of these two data sources was evaluated through comparisons of the time series, bulk wave statistics and wave energy spectra with the DWR-G estimates.

An example of the horizontal easting displacement time series (see Figure 27) illustrates the excellent agreement between the GT-31 DGPS displacements and the DWR-G displacements (see also Pearman et al. 2013). The peaks of the signals track well.

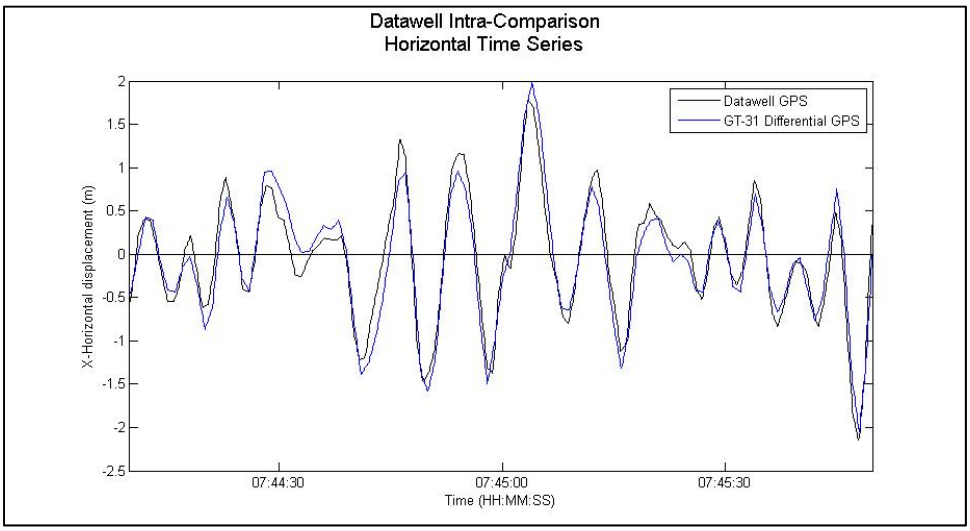

Figure 27. Displacement time series of DWR-G and GT-31 easting displacements.

The bulk wave statistics from the various horizontal surface motions are listed in Table 11 for comparison. Statistics from the GT-31 DGPS displacements agreed extremely well with the DWR-G displacements. The significant wave height differed by less than 2% (0.04m) and the mean wave direction was identical to that calculated by the DWR-G buoy. The mean wave period differed by approximately 6% (0.13sec) from the DWR-G buoy. The largest difference was observed in the directional spread, which differed by approximately 7% (~1.5°) from the DWR-G buoy.

Overall, the bulk wave statistics from the GT-31 Doppler velocities also agreed very well with the DWR-G displacements. The significant wave height had slightly higher error than that calculated from the GT-31 DGPS displacements, but was still within approximately 4% (0.14m) of the DWR-G buoy. The mean wave period differed by less than 4% (0.28sec) and the mean wave direction differed by less than 0.1°. Similar to the GT-31 DGPS displacements, the directional spread was within approximately 7% (~1.5°) of the DWR-G buoy.

Table 11. Bulk wave statistics calculated from the two horizontal positioning methods are compared with the DWR-G results.

Horizontal Positioning Comparison					
Positioning source	DWR-G Displacements	GT-31 DGPS Displacements	Diff	GT-31 Doppler Velocities	Diff
Significant wave height (m)	3.43	3.39	-1.21 %	3.57	4.11 %
Mean wave period (sec)	8.4	8.9	6.15 %	8.7	3.31 %
Mean wave direction (deg)	310	310	0.01°	310	0.08°
Directional spread (deg)	21	22	1.47°	22	1.47°

A spectral comparison of the two horizontal positioning techniques of the GT-31 was also performed following the methods in Pearman et al. (2013). The wave energy spectra (top panel of Figure 28) were calculated using the horizontal surface motions from the DWR-G, the GT-31 DGPS displacements and the GT-31 Doppler velocities. All three estimates have similar spectral characteristics and spectral energy levels, particularly between 0.085Hz – 0.18Hz, which encompasses the typical swell-sea band. At frequencies below 0.085Hz (long period waves), both GT-31 estimates have higher spectral energy levels compared to the DWR-G. At frequencies above 0.18Hz (short period waves), the GT-31 DGPS displacements observe reduced spectral energy levels, while the GT-31 Doppler velocities observe similar spectral energy levels as the DWR-G.

Spectral estimates of the mean wave direction calculated from 2nd-order Fourier moments are compared in the middle panel of Figure 28. All three estimates agree extremely well for frequencies between 0.078Hz – 0.24Hz. At frequencies less than 0.078Hz, the DWR-G directional spectra has some erratic direction observations, which are likely due to the 180° ambiguity introduced by the 2nd-order Fourier moments as

noted by Herbers et al. (2012). At frequencies above 0.24Hz the GT-31 DGPS displacements show more variability than the DWR-G and the GT-31 Doppler velocities.

Spectral estimates of the directional spread calculated from 2nd-order Fourier moments are compared in the bottom panel of Figure 28. The three estimates show similar variations with frequency, with the narrowest spread near the 0.1Hz swell peak frequency. At higher and lower frequencies, both GT-31 estimates are biased high by a few degrees relative to the DWR-G.

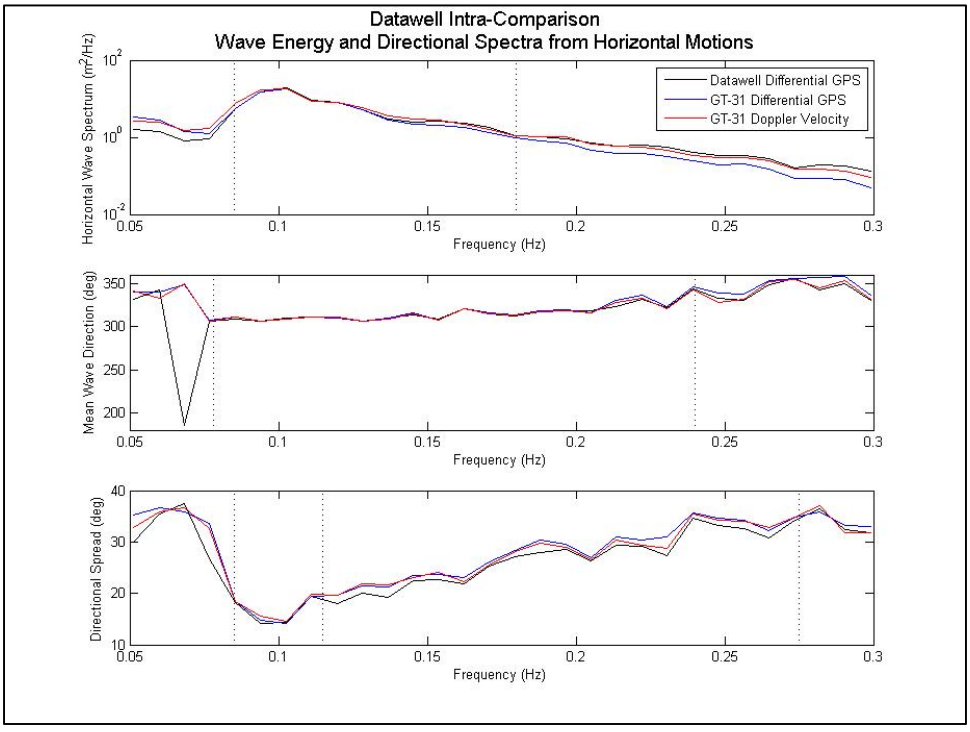

Figure 28. Wave spectra calculated from horizontal surface motions. Top panel: wave energy spectra. Middle panel: mean wave direction. Bottom panel: directional spreading.

This confirms the results from Herbers et al. (2012) that the GT-31 DGPS displacements can provide similar bulk wave statistics and spectra as that of the DWR-G, particularly in the swell-sea frequency band. This analysis also shows that the statistics and spectra calculated from the GT-31 Doppler velocities are in excellent agreement with the DWR-G estimates. Further, the GT-31 Doppler velocities perform better than the GT-

31 DGPS displacements at higher frequencies, making this horizontal positioning technique more advantageous for observing the wave-induced surface motion across a wide frequency range.

3. Vertical Wave Motion

The sensor configuration developed for the WRD provided two different techniques for measuring the vertical surface motions of the waves: traditional DGPS displacements and vertical accelerations. Similar to the horizontal positioning, the performance of these two techniques was compared to that of the well-tested DWR-G.

A plot of the vertical displacement time series from the three sensors is shown in Figure 29. All three estimates show the same phase evolution, but there are large differences in the amplitude of the waves. The DWR-G displacements and the X6–2 acceleration-based estimates agree well with some tendency for the X6–2 accelerations to yield larger wave heights. The faster sampling rate of the accelerometer compared to the DWR-G buoy may contribute to these differences by better resoling the wave crests. On the other hand, the accelerometer-based wave heights may be biased high by uncorrected slope errors (see Pearman et al. 2013 for more discussion). Conversely, the GT-31 DPGS measures significantly lower wave amplitudes as compared to the DWR-G buoy (Pearman et al. 2013). This is likely due to the poor vertical resolution of the single frequency GPS receiver in the GT-31.

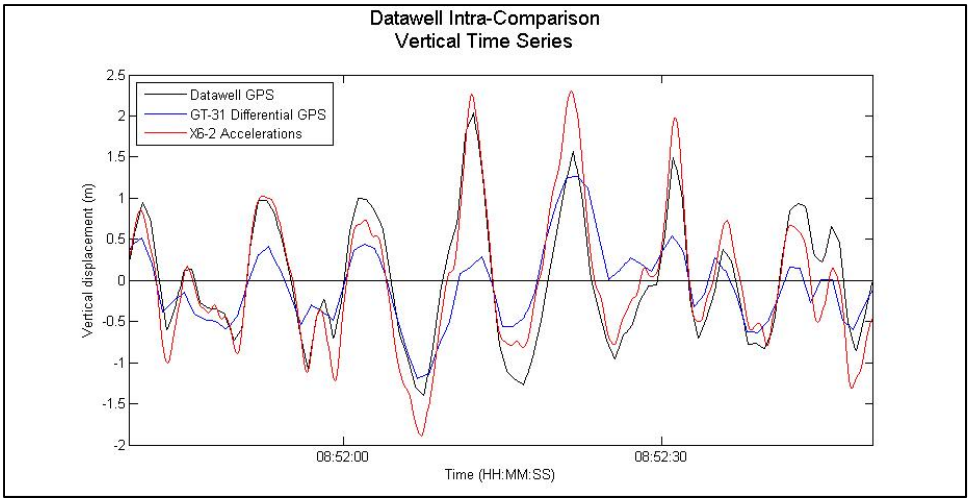

Figure 29. Vertical displacement time series.

Statistics of the measured vertical surface motions are listed in Table 12 for comparison. Bulk wave statistics from the GT-31 DGPS displacements showed extremely poor agreement with the DWR-G displacements. The significant wave height is biased low almost 45% (1.5m) as compared to that calculated by the DWR-G buoy. Significant errors are also noted in the mean wave period (10%, 0.83sec) and directional spread (51%, 13.7°). However, the mean wave direction differs by only 1.3° from the direction measured by the DWR-G buoy, indicating that the phase evolution of the wave field is still well resolved.

The bulk wave statistics from the X6–2 accelerations are in much better agreement with the DWR-G buoy. The significant wave heights differed by less than 6% (0.19m) and the mean wave period and the mean wave direction also agree well. On the other hand, the directional spread is almost 28% (7.42°) higher than the DWR-G buoy estimate, suggesting higher noise levels in the accelerometer measurements.

Table 12. Bulk wave statistics calculated from the three vertical positioning methods with differences compared to the DWR-G displacements.

Vertical Positioning Comparison					
Positioning source	DWR-G Displacements	GT-31 DGPS Displacements	Diff	X6-2 Accelerations	Diff
Significant wave height (m)	3.37	1.87	-44.37 %	3.56	5.60 %
Mean wave period (sec)	8.3	9.1	9.99 %	8.1	-2.16 %
Mean wave direction (deg)	309	308	-1.30°	309	-0.18°
Directional spread (deg)	27	41	13.74°	34	7.42°

A spectral comparison of the two vertical positioning techniques was also performed following the methods in Pearman et al. (2013). The wave energy spectra (top panel of Figure 30) were calculated using the vertical surface motions from the DWR-G, GT-31 DGPS displacements and X6–2 accelerations. All three positioning techniques have similar spectral characteristics; however they differ in their spectral energy levels. The DWR-G and the X6–2 accelerations agree very well for frequencies between 0.08Hz – 0.18Hz, but diverge slightly at frequencies greater than 0.18Hz (short period waves), where the X6–2 accelerations yield a slightly more energetic spectrum, possibly because the X6–2 accelerometer is more sensitive to nonlinear (i.e. near breaking) high frequency waves. Conversely, the GT-31 DGPS displacements show much lower spectral energy levels at all frequencies in the wind wave and swell band (Herbers et al. 2012 and Pearman et al. 2013).

Spectral estimates of the mean wave direction calculated from 1st-order Fourier moments are compared in the middle panel of Figure 30. Generally, all three estimates of the mean wave direction agree well. At frequencies less than 0.075Hz, where energy levels are relatively low, there are large discrepancies. Neither of the WRD vertical measurement techniques accurately compare to the DWR-G at these low frequencies. At frequencies greater than 0.22Hz, the X6–2 accelerations agree well with the DWR-G displacements, while the GT-31 DGPS displacements show some variability in direction.

Spectral estimates of the directional spread calculated from 1st-order Fourier moments are compared in the bottom panel of Figure 30. The directional spread shows large variability in the degree of spread among the three positioning techniques. The GT-31 DGPS displacements and X6–2 accelerations observe consistently larger spreading

across the entire frequency band as compared to the DWR-G displacements. However, the X6–2 acceleration spectrum does agree better than the GT-31 DGPS displacement spectrum, particularly for frequencies greater than 0.08Hz.

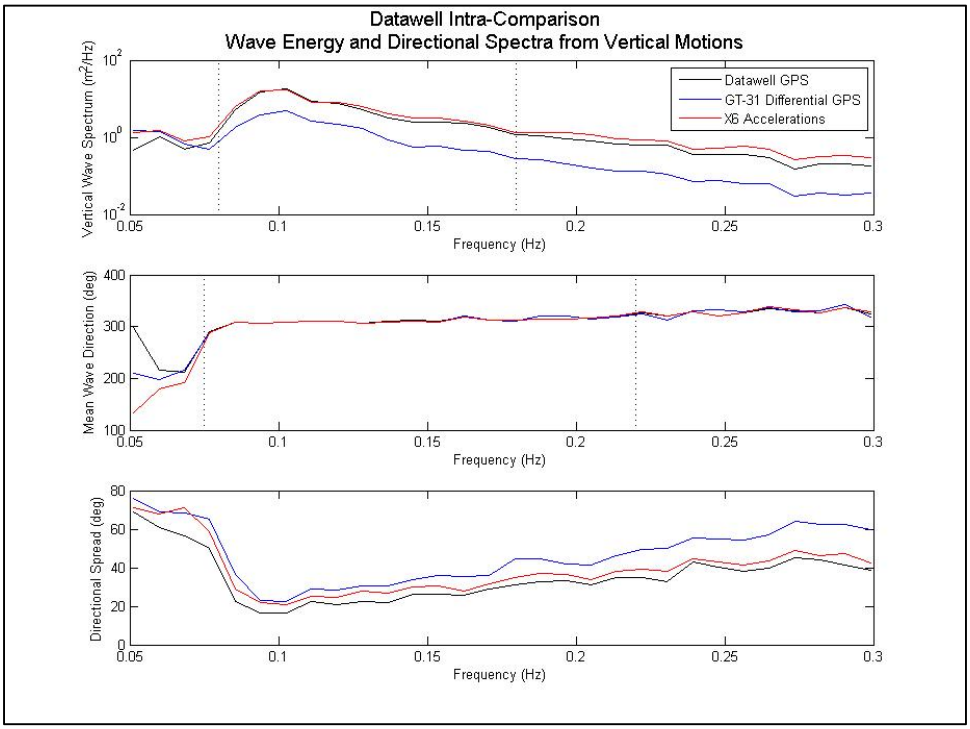

Figure 30. Wave spectra calculated from vertical surface motions. Top panel: wave energy spectra. Middle panel: mean wave direction spectra. Bottom panel: directional spreading.

This analysis shows that the bulk wave statistics and wave energy spectra calculated using the GT-31 DGPS vertical displacements do not compare well to those calculated by the DWR-G buoy, which is consistent with previous results from Herbers et al. (2012). However, these results show that the X6–2 accelerometer does provide reliable observations of the vertical wave-induced surface motion, which can be used in conjunction with the GT-31 horizontal measurements to obtain bulk wave statistics and wave spectra.

Overall, the combined use of the horizontal Doppler velocities from the GT-31 GPS receiver and the vertical accelerations from the X6–2 accelerometer provide an

accurate and reliable sensor configuration for observing the wave-induced fluid motions. Collocated on the same buoy, these sensors accurately observe the surface motions in the swell and wind-wave frequency band, producing robust wave and spectral statistics that are similar to those provided by widely used Datawell buoys.

C. INTER-BUOY COMPARISON: DWR-G VS. WRD

The second step of the validation involved a statistical and spectral comparison of the WRD buoy design. Three WRD buoys and one DWR-G buoy were outfitted with the same sensor configuration and were deployed in the same homogenous deep-water wave field.

The sensor validation showed that the most reliable statistics for the swell-sea and wind-wave frequency band were obtained using the GT-31 horizontal Doppler velocities in conjunction with X6–2 vertical accelerations. The three WRD buoys (A06, A08 and A17) were processed using these data streams. In addition, the GT-31 and X6–2 sensor configuration onboard the DWR-G was also included in the analysis and processed the same way as the stand-alone WRD buoys.

Statistics calculated from the DWR-G and WRD buoys using the same sensors (GT-31 and X6-2) are listed in Table 13 for comparison. The bulk wave statistics from all three WRD buoys agreed very well with the statistics calculated from the DWR-G. The significant wave height calculated by the WRD buoys differed by an average of less than 7% (0.24m) when compared to the DWR-G buoy. Other wave parameters show similar good agreement with differences of 2% (0.13sec) for the mean wave period, less than 1° for the mean wave direction, and 6% (1.5°) for the directional spread, as compared to the DWR-G buoy.

The bulk wave statistics showed little difference between those calculated from vertical surface motions and those calculated from horizontal surface motions. The average significant wave height of the WRD buoys calculated from vertical motions was within 6% (0.21m) of the DWR-G buoy while that calculated from horizontal motions was within 7.5% (0.27m). Similarly, the average directional spread of the WRD buoys

calculated from vertical motions was within 5% (1.6°) of the DWR-G buoy while the directional spread calculated from horizontal motions was within 6% (1.4°).

Table 13. Bulk wave statistics calculated from the three WRD buoys and DWR-G buoy using GT-31 Doppler velocities and X6–2 accelerations with differences compared to the DWR-G buoy.

WRD COMPARISON to DWR-G (Doppler velocity/Accelerations)									
Vertical Orbital Motions	**Datawell**	**WRD-A06**	**Diff**	**WRD-A08**	**Diff**	**WRD-A17**	**Diff**	**WRD Average**	**Diff**
Significant wave height (m)	3.56	3.78	6.19 %	3.69	3.65 %	3.85	8.16 %	3.77	6.00 %
Mean wave period (sec)	8.1	8.4	4.34 %	8.2	1.79 %	8.2	2.14 %	8.3	2.75 %
Mean wave direction (deg)	309	311	1.95°	310	1.47°	309	0.03°	310	1.15°
Directional spread (deg)	34	32	-2.13°	34	-0.40°	32	-2.37°	33	-1.63°
Horizontal Orbital Motions	**Datawell**	**WRD-A06**	**Diff**	**WRD-A08**	**Diff**	**WRD-A17**	**Diff**	**WRD Average**	**Diff**
Significant wave height (m)	3.57	3.34	-6.53 %	3.19	-10.83 %	3.39	-5.18 %	3.31	-7.51 %
Mean wave period (sec)	8.7	8.7	0.27 %	8.6	-0.88 %	8.7	-0.34 %	8.7	-0.32 %
Mean wave direction (deg)	310	312	1.71°	311	0.64°	310	-0.26°	311	0.70°
Directional spread (deg)	22	21	-1.60°	21	-0.68°	20	-1.83°	21	-1.37°

A further comparison of the bulk wave statistics showed that the average statistics calculated from the WRD buoys compared very well to the statistics calculated from the DWR-G displacements (see Table 14). The average significant wave height of the WRD buoys was with 12% (0.40m) when compared to the significant wave height from the DWR-G displacements. The larger positive bias (compared with Table 13) shows that both the buoy response and the sensor characteristics contribute to these differences. The average wave period, wave direction and directional spread of the WRD buoys are within 1% (0.16sec), 1° and 6° respectively, when compared to the statistics from the DWR-G displacements.

Table 14. Bulk wave statistics calculated from the three WRD buoys using GT-31 Doppler velocities and X6–2 accelerations with differences compared to the DWR-G DGPS displacements.

WRD COMPARISON to DWR-G (Displacements)									
Vertical Orbital Motions	**Datawell**	**WRD-A06**	**Diff**	**WRD-A08**	**Diff**	**WRD-A17**	**Diff**	**WRD Average**	**Diff**
Significant wave height (m)	3.37	3.78	12.14 %	3.69	9.46 %	3.85	14.22 %	3.77	11.94 %
Mean wave period (sec)	8.3	8.4	2.09 %	8.2	-0.41 %	8.2	-0.06 %	8.3	0.54 %
Mean wave direction (deg)	309	311	1.77°	310	1.30°	309	-0.15°	310	0.97°
Directional spread (deg)	27	32	5.29°	34	7.02°	32	5.05°	33	5.79°
Horizontal Orbital Motions	**Datawell**	**WRD-A06**	**Diff**	**WRD-A08**	**Diff**	**WRD-A17**	**Diff**	**WRD Average**	**Diff**
Significant wave height (m)	3.43	3.34	-2.69 %	3.19	-7.16 %	3.39	-1.28 %	3.31	-3.71 %
Mean wave period (sec)	8.4	8.7	3.59 %	8.6	2.40 %	8.7	2.96 %	8.7	2.99 %
Mean wave direction (deg)	310	312	1.79°	311	0.72°	310	-0.18°	311	0.77°
Directional spread (deg)	21	21	-0.13°	21	0.79°	20	-0.36°	21	0.10°

A spectral comparison of the three WRD buoys and the DWR-G buoy was also performed following the methods in Pearman et al. (2013). Spectra calculated from vertical surface motions are shown in Figure 30. The vertical wave energy spectrum (top panel of Figure 31) was calculated using the surface motions from the DWR-G displacements and the X6-2 accelerations on the WRD buoys. The DWR-G, WRD-A06, WRD-A08 and WRD-A17 buoys show excellent agreement in spectral peaks, characteristics and spectral energy levels for frequencies greater than 0.08Hz. At frequencies less than 0.08Hz, the WRD buoy spectra show similar spectral energy levels that are higher than the DWR-G estimates.

Spectral estimates of the mean wave direction calculated from 1st-order Fourier moments are compared in the middle panel of Figure 31. Again, the WRD buoys and DWR-G buoy show excellent agreement for all frequencies greater than 0.075Hz. At frequencies less than 0.075Hz, the directional spectra for all four buoys diverge indicating that this sensor and buoy configuration cannot accurately resolve these long-period swell directions.

Finally, spectral estimates of the directional spreading calculated from 1st-order Fourier moments are compared in the bottom panel of Figure 31. Again, the WRD buoys and DWR-G buoy spectra show excellent agreement for all frequencies greater than 0.065Hz. At frequencies less than 0.065Hz, the WRD buoys agree well with each other, but display slightly higher degrees of spreading than the DWR-G.

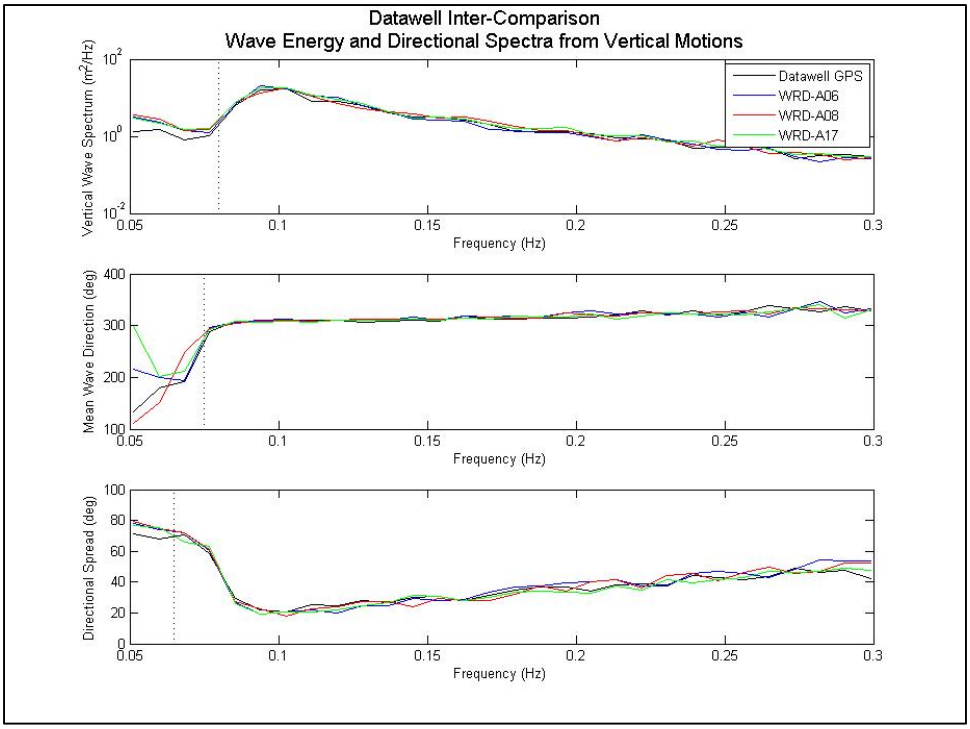

Figure 31. Wave spectra calculated from vertical surface motions. Top panel: wave energy spectra. Middle panel: mean wave direction spectra. Bottom panel: directional spreading.

Spectra calculated from horizontal surface motions are shown in Figure 32. The horizontal wave energy spectra (top panel of Figure 32) were calculated using the horizontal DWR-G displacements and GT-31 Doppler velocities, applying the linear transfer functions from Table 6. Similar to the vertical spectra, the DWR-G buoy, WRD-A06, WRD-A08 and WRD-A17 show excellent agreement in spectral peaks, characteristics and spectral energy levels for the entire frequency band. There is some variability at frequencies less than 0.07Hz and greater than 0.25Hz where the DWR-G spectrum has slightly higher spectral energy levels.

Spectral estimates of the mean wave direction calculated from 2nd-order Fourier moments are compared in the middle panel of Figure 32. Again, the WRD buoys and DWR-G buoy show excellent agreement for frequencies between 0.08Hz – 0.2Hz. Unlike the vertical motions, the horizontal motions show greatly improved agreement at low frequencies (less than 0.08Hz); however, they also show larger variability at frequencies greater than 0.2Hz.

Finally, spectral estimates of the directional spreading calculated from 2nd-order Fourier moments are compared in the bottom panel of Figure 32. Again, the WRD buoys and DWR-G buoy spectra show good agreement in their spectral characteristics across the entire frequency band; however, there is increased variability at frequencies greater 0.085Hz.

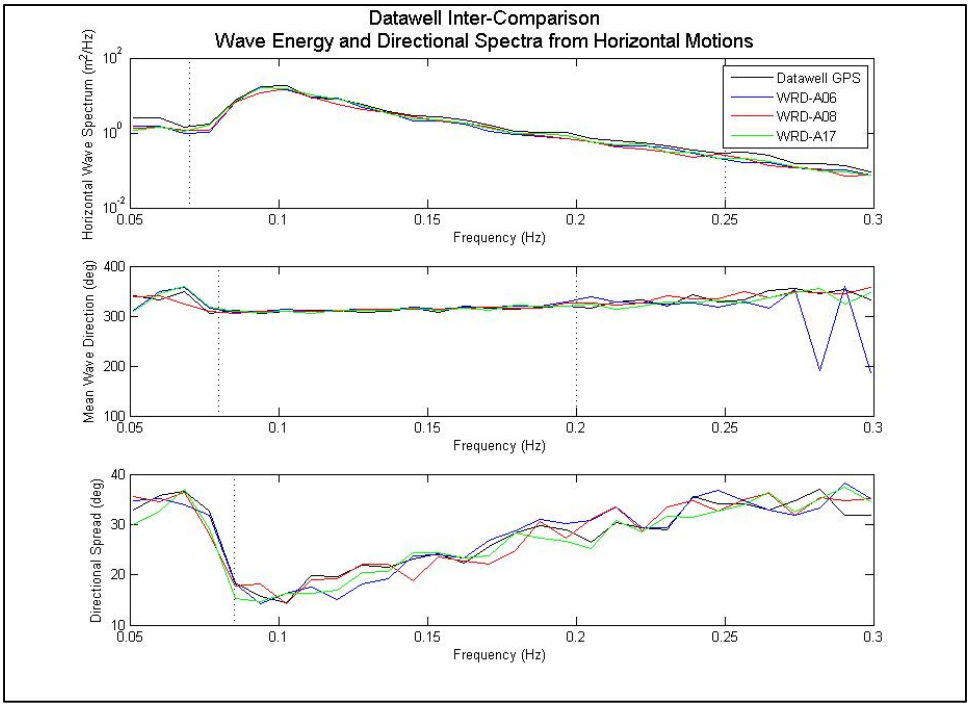

Figure 32. Wave spectra calculated from horizontal surface displacements. Top panel: wave frequency spectra. Middle panel: mean wave direction spectra. Bottom panel: directional spreading.

The statistical and spectral comparison confirms that the WRD buoy and sensor configuration provides similar bulk wave statistics and wave spectra as the widely used DWR-G buoys, particularly in the dominant swell and wind-wave frequency band (0.07-0.25Hz). Table 15 summarizes the WRD system performance compared to the DWR-G. The total system performance is comprised of errors/bias introduced by the sensor configuration (evaluated in Section 4.A) and the buoy design (evaluated in Section 4.B). The overall system performance is slightly better using horizontal surface motions; however, the vertical surface motions still provide adequate statistics as well. The

significant wave height calculated from the horizontal motions is within 3.7% of the DWR-G while the wave height calculated from the vertical motions is within 12% of the DWR-G.

Table 15. WRD system performance.

System Performance Comparison			
Sensor Configuration	Sensor Performance DWR-G (GPS) vs. DWR-G (Doppler Velocity / Acceleration)	Buoy Performance DWR-G (Doppler Velocity / Acceleration) vs. WRD (Doppler Velocity / Acceleration)	System Performance DWR-G (GPS) vs. WRD (Doppler Velocity / Acceleration)
Vertical Motions			
Significant wave height (m)	5.60 %	6.00 %	11.94 %
Mean wave period (sec)	-2.16 %	2.75 %	0.54 %
Mean wave direction (deg)	-0.18°	1.15°	0.97°
Directional spread (deg)	7.42°	-1.63°	5.79°
Horizontal Motions			
Significant wave height (m)	4.11 %	-7.51 %	-3.71 %
Mean wave period (sec)	3.31 %	-0.32 %	2.99 %
Mean wave direction (deg)	0.08°	0.70°	0.77°
Directional spread (deg)	1.47°	-1.37°	0.10°

THIS PAGE INTENTIONALLY LEFT BLANK

V. APPLICATION OF WRD BUOY IN THE NEARSHORE

The WRD buoys were validated to provide similar bulk wave statistics and spectra as the DWR-G in a homogenous offshore wave field. In order to examine their applicability in the nearshore environment, an array of WRD buoys was deployed on four cruises within the Golden Gate channel and the mouth of San Francisco Bay. These buoys drifted with the surface tidal current and observed the spatial and temporal evolution of the wave field across this dynamic nearshore environment. Two of the four nearshore deployments are discussed here.

A. DRIFTER TRACKS

The first nearshore deployment was conducted on February 15, 2012. 20 WRD buoys were deployed from underneath the Golden Gate Bridge on an ebb-tidal current and allowed to drift out of the channel with the current; however only 13 WRD buoys were recovered at various times over the next 24 hours. WRD deployment and retrieval times are listed in Table 16 along with the applicable tidal currents that each buoy experienced.

Table 16. February 15 WRD buoy deployment times.

February 15, 2012 Drifter Deployment									
Buoy	Deploy		Recover		Tidal Current				
	Date	Time	Date	Time					
WRD-A01	2/15	15:13	2/16	16:28	Ebb #1	Flood #1	Ebb #2	Flood #2	Ebb #3
WRD-A02	2/15	15:27	2/16	17:13	Ebb #1	Flood #1	Ebb #2	Flood #2	Ebb #3
WRD-A03	2/15	15:39	2/16	16:23	Ebb #1	Flood #1	Ebb #2	Flood #2	Ebb #3
WRD-A04	2/15	15:50	Lost		X	X	X	X	X
WRD-A06	2/15	16:00	2/16	17:23	Ebb #1	Flood #1	Ebb #2	Flood #2	Ebb #3
WRD-A07	2/15	16:10	2/16	14:56	Ebb #1	Flood #1	Ebb #2	Flood #2	
WRD-A08	2/15	16:20	Lost		X	X	X	X	X
WRD-A09	2/15	16:31	Lost		X	X	X	X	X
WRD-A10	2/15	16:41	2/15	22:32	Ebb #1	Flood #1	X	X	X
WRD-A11	2/15	16:50	2/15	22:54	Ebb #1	Flood #1	X	X	X
WRD-A12	2/15	17:02	2/15	21:38	Ebb #1	Flood #1	X	X	X
WRD-A13	2/15	17:11	Lost		X	X		X	X
WRD-A14	2/15	17:20	2/16	07:53	Ebb #1	Flood #1	Ebb #2	X	X
WRD-A15	2/15	17:30	2/15	23:21	Ebb #1	Flood #1	X	X	X
WRD-A16	2/15	17:41	2/16	01:33	Ebb #1	Flood #1	X	X	X
WRD-A17	2/15	17:50	2/15	20:31	Ebb #1	X	X	X	X
WRD-A18	2/15	18:00	Lost		X	X		X	X
WRD-A19	2/15	18:10	2/16	00:24	Ebb #1	Flood #1	X	X	X
WRD-A20	2/15	18:21	Lost		X	X		X	X
WRD-A21	2/15	18:31	Lost		X	X		X	X

The drift tracks for this deployment are shown in Figure 33. Since the predominant wind was out of the NW (318°) at 10m/s, the drift tracks demonstrate that the buoys were well coupled to the surface current and not strongly affected by the wind. This deployment demonstrates the possibility of utilizing a large array of these Lagrangian drifters in order to observe the spatial evolution of the wave field in the nearshore environment, particularly the interaction with bathymetry and variable surface tidal currents.

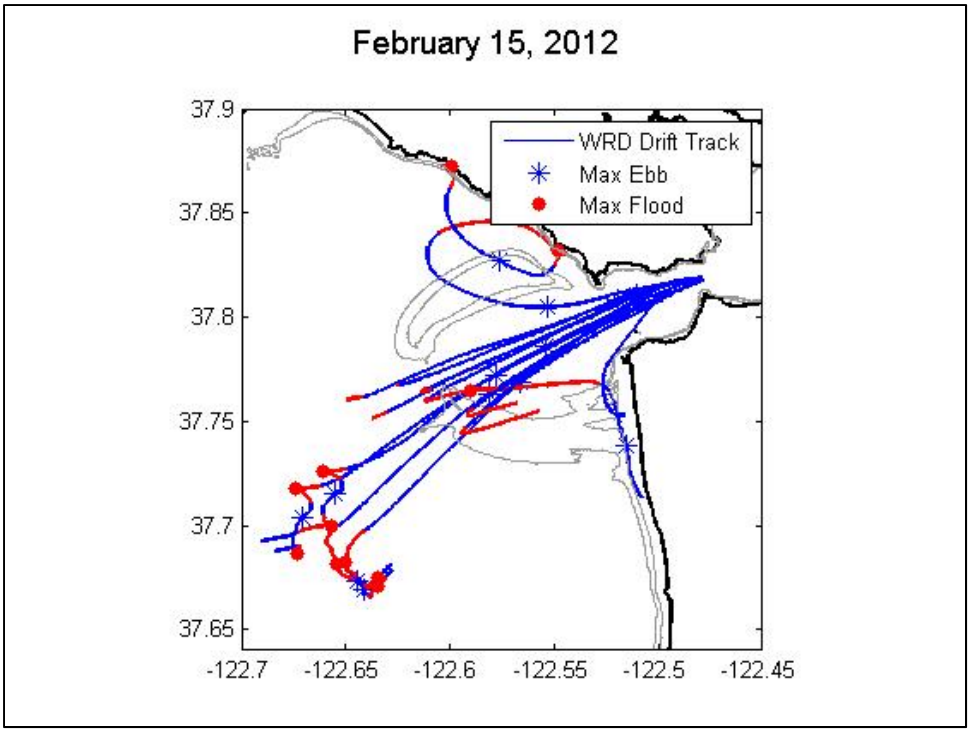

Figure 33. Buoy drift tracks from the February 15 deployment indicating the tidal stage on the drift tracks.

WRD-A01, WRD-A02, WRD-A03 and WRD-A06 were deployed first and experienced the strongest ebb current. These buoys drifted out of the channel and well past the ebb-tidal shoal before the ebb current abated. Offshore of the ebb-tidal shoal, the currents were weak, and all four of these buoys remained offshore, oscillating in successive flood and ebb currents. However, none of these currents were strong enough to bring the buoys back toward shore.

Conversely, WRD-A14, WRD-A16 and WRD-A19 were deployed later in the day, on a weaker ebb current. These buoys only drifted out as far as the ebb-tidal shoal before the tide shifted. The subsequent flood current near the shoal was strong enough to affect the buoys, bringing them back toward the channel before WRD-A16 and WRD-A19 were retrieved.

WRD-A14 continued to drift toward shore on the flood current. This buoy was close enough to shore during the next tide change, that during this ebb current, the buoy began drifting in an alongshore current south of the channel. This southward flowing

alongshore current is also seen in the drift track of WRD-A17 which drifted south as it exited the channel on the initial ebb current. These two buoy drift tracks identify an ebb-tidally driven alongshore current south of the channel discussed in Shi et al. (2011).

On the north side of the channel, WRD-A07 drifted north on the initial ebb current as it exited the channel and drifted out over the ebb-tidal shoal. As the tide changed, the buoy drifted back toward shore on the flood current. It continued to drift southeastward with the flood current moving in and out of the surf zone, until it drifted offshore with the next ebb current. The buoy drifted offshore and northwestward during the ebb current. This buoy drift track identifies a tidally-driven eddy circulation that forms over the northern reach of the ebb-tidal shoal outside of the channel.

B. SPATIAL VARIABILITY ANALYSIS

1. February 15, 2012

The data from this deployment was analyzed for the period of the first ebb current (15:14 UTC – 21:36 UTC). The buoy drift tracks show the spatial coverage of the WRD array during this time (see Figure 34). In order to study some of the dynamic features of the nearshore environment, five distinct spatial regions of the dataset were identified: offshore of the ebb-tidal shoal, over the ebb-tidal shoal, inshore of the ebb-tidal shoal, in the vicinity of Mile Rock (the entrance to the Golden Gate channel) and inside the channel (see Figure 34). These regions were identified for having similar wave statistics. The bulk wave statistics for these regions were averaged for all of the available WRD buoys and are listed in Table 17.

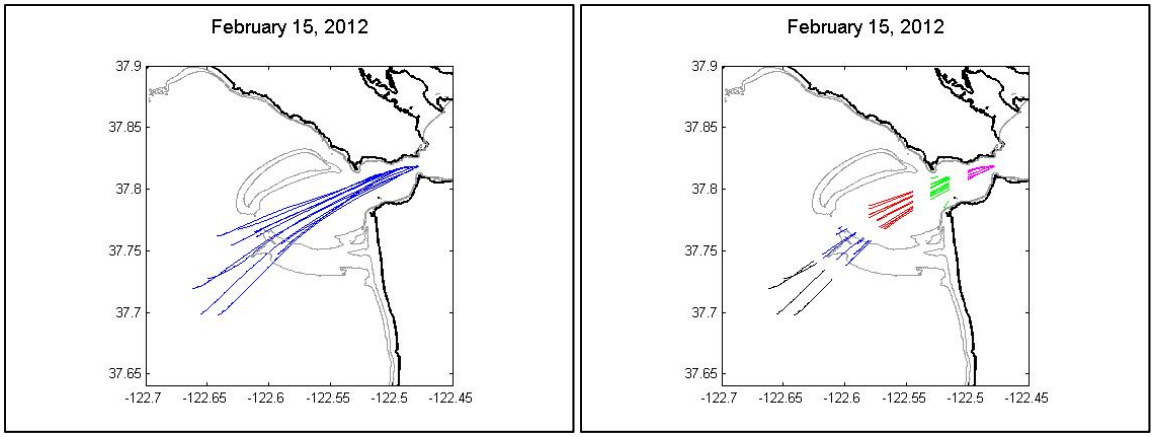

Figure 34. Buoy drift tracks from the February 15 deployment. The left panel shows the overall spatial distribution. The right panel indicates the five spatial regions.

Table 17. Bulk wave statistics averaged over all of the WRD buoys for the five spatial regions of the February 15 deployment.

WRD Golden Gate Drift Deployment – Feb 15, 2012										
Vertical Orbital Motions	Offshore		Shoal		Inshore		Channel Entrance		Channel	
	Mean	Std Dev	Mean	Std Dev	Mean	Std Dev	Mean	Std Dev	Mean	Std Dev
Depth (m)	27		12		20		40		92	
Mean drift rate (m/s)	0.5		0.9		1.2		1.5		1.6	
Significant wave height (m)	2.52	0.04	2.79	0.24	2.22	0.14	1.84	0.27	1.48	0.22
Mean wave period (sec)	8.5	0.10	9.7	0.87	8.1	0.39	8.0	0.71	7.8	0.87
Mean wave direction (deg)	280	1.72	274	3.30	276	3.80	277	3.91	295	6.47
Directional spread (deg)	34	2.11	31	2.23	39	3.10	40	3.67	46	6.74

The buoys drifted out the channel, in the opposite direction of the approaching wave field. The offshore wave field (measured by NDBC station 46026) is characterized by a significant wave height of approximately 2.7m coming out of the WNW (286°) during this deployment period (from Table 4).

As the wave field propagates from offshore to over the ebb-tidal shoal, the average water depth decreases significantly from 27m to 12m. The tidal current offshore of the shoal is relatively weak as evidenced by a low buoy drift rate of 0.5m/s (1.0kts). The significant wave height in this region increases by 0.27m. This is qualitatively consistent with the linear shoaling effect resulting in an increase of wave energy due to the decreasing group speed over the shoal. Additionally, the mean wave direction in this region changes slightly by coming from 280° to coming from 274°. This appears

consistent with refraction over the bathymetry as the wave field propagates over the dredged channel and onto the ebb-tidal shoal.

As the wave field propagates past the shoal, the average water depth increases from 12m to 20m and the ebb-tidal current steadily increases, reaching an average speed of 2.3kts (using the buoy drift rate). The significant wave height decreases by 0.57m in this region which is consistent with bathymetric effects of the shoal. Much of the swell energy is likely dissipated over the shoal (Pearman et al. 2013) and the shoaling effect reverses as the wave field propagates towards deeper water. The mean wave direction only slightly changes direction back to coming from 276°. The directional spreading in this region also increases by 8° in this region. Since the bathymetry of the shoal continues to the southeast, these two directional effects suggest that the wave field over the southern reach of the shoal is beginning to refract back toward the channel and onto the opposing ebb-tidal current.

As the wave field propagates toward the channel entrance, the average water depth continues to increase (to 40m) while the ebb-tidal current also continues to increase in strength, reaching an average speed of 2.9kts. The significant wave height in this region decreases by 0.38m while the mean wave direction and directional spreading remain constant from the inshore region. There is no obvious signature of any expected wave-current interactions, and the temporal and spatial variability of the tidal currents complicate the analysis in this region. The buoy observations occurred during peak ebb currents (early in the deployment), and very weak ebb currents (toward the end of the deployment). Additionally, the buoy drift tracks encompassed nearly the entire width of the channel, capturing observations inside the tidal jet, and the northern and southern boundaries of the jet.

Finally, as the wave field propagates into the center of the channel, the average water depth increases significantly (to 92m) and the ebb current reaches its strongest speed, increasing to 3.1kts (from buoy drift rate). The significant wave height again decreases by 0.36m, which is consistent with the decrease in wave energy as the wave field spreads out, traveling faster in the deeper water of the channel. Inside the channel, the mean wave direction changes nearly 20° to the southeast (coming from 295°) as the

waves begin to exhibit some refractive effects from the nearby coastline. The directional spreading of the wave field also increases by 6° as the waves react to the refractive effects of the coastline as well as some refractive effects from the ebb current, which is strongest for all of the buoys in this region.

2. April 27, 2012

The second nearshore deployment was conducted on April 27, 2012. Similar to the February deployment, a large array of 29 WRD buoys was deployed from underneath the Golden Gate Bridge. However, during this deployment, the buoys were deployed in the center of the tidal jet as measured by the ADCP onboard R/V Questuary. The buoy drift tracks show the spatial coverage of the WRD array (see Figure 34). This deployment provided a unique synoptic view of the wave field as it progressed from offshore. The data was analyzed for the same five spatial regions used for the February dataset (see Figure 35). The bulk wave statistics for these regions were averaged for all of the applicable WRD buoys and are listed in Table 18.

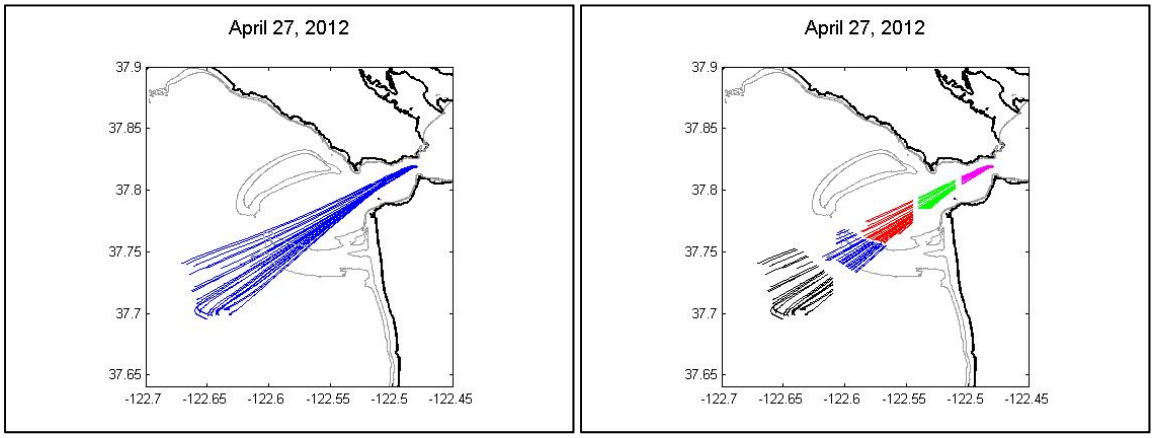

Figure 35. Buoy drift tracks from the April 27 deployment. The left panel shows the overall spatial distribution. The right panel indicates the five spatial regions.

Table 18. Bulk wave statistics averaged over all of the WRD buoys for the five spatial regions of the April 27 deployment.

WRD Golden Gate Drift Deployment – Apr 27, 2012										
Vertical Orbital Motions	Offshore		Shoal		Inshore		Channel Entrance		Channel	
	Mean	Std Dev	Mean	Std Dev	Mean	Std Dev	Mean	Std Dev	Mean	Std Dev
Depth (m)	28		12		19		36		97	
Mean drift rate (m/s)	0.7		1.4		1.8		1.9		1.6	
Significant wave height (m)	2.51	0.11	2.80	0.57	2.14	0.51	2.24	0.44	1.61	0.15
Mean wave period (sec)	8.7	0.32	8.5	0.31	7.0	0.41	6.8	0.22	6.9	0.24
Mean wave direction (deg)	277	2.46	273	1.94	273	1.89	283	2.58	305	2.50
Directional spread (deg)	35	2.79	31	1.81	40	3.88	36	2.93	36	4.87

The offshore wave field measured by NDBC Station 46042 was similar to February 15, 2012 with a significant wave height of 2.6m and a wave field coming out of the WNW (288°) (from Table 5). Again, the buoys were well coupled to the surface current as the buoys drifted straight out of the channel despite having prevailing surface winds of 11m/s out of the northwest (315°).

As the wave field propagates from offshore to over the shoal, the average water depth decreases significantly from 28m to 12m. Again, the offshore current is relatively weak as evidenced by a buoy drift rate of 0.7m/s (1.4kts). Similar to the February deployment, the significant wave height increases by 0.29m as the wave field propagates over the shoal as a result of the bathymetric interaction. The mean wave direction changes slightly by turning nearly 4° to the east (coming from 273°) and the directional spreading narrows by more than 4°. These directional changes are qualitatively consistent with refraction over the shoal.

As the wave field propagates off the shoal, the average water depth increases from 12m to 19m. The effects of the ebb-tidal current begin to increase as the buoy drift rate increases to 1.8m/s (3.5kts). Similar to February, the significant wave height decreases by 0.66m as much of the swell energy is dissipated from the bathymetric interaction of the shoal (Pearman et al. 2013). The decrease in swell energy is also observed in a decrease in the mean wave period from 8.5sec to 7sec indicating that the wave field has diminished contributions from long-period swell. As seen in February, the wave directions do not continue to refract to the southeast along the shoal; instead, the mean wave direction remains eastward (coming from 273°). This lack of directional change

accompanied with a 9° increase in the directional spread indicates influence of the opposing ebb-tidal current resulting in the wave field refracting back toward the current.

As the wave field propagates toward the channel entrance, the water depth continues to increase (to 36m), while the ebb current reaches its maximum speed of 1.9m/s (3.7kts) indicating that the ebb-tidal current is strongest in this region. The mean wave direction changes by 10° (coming from 283°) as the wave field observed by the buoys refracts into the channel. This results in the wave field propagating against the strong, ebb current. The effects of the ebb current are also exhibited in the 4° narrowing of the directional spreading, indicating that the wave field is refracting in on the current.

Finally, as the wave field propagates into the center of the channel, the water depth increases significantly (to 97m) and the buoy drift rate abates slightly to 1.6m/s (3.1kts). Much of the wave energy has either been dissipated or blocked by the opposing ebb current at the channel entrance, which results in a 0.63m decrease in the significant wave. The mean wave direction continues to change by nearly 20° (coming from 305°) inside the channel, possibly owing to sheltering effects of the nearby coastline.

THIS PAGE INTENTIONALLY LEFT BLANK

VI. CONCLUSIONS

The nearshore environment, particularly around a narrow tidal inlet, provides many challenges for observing ocean waves with traditional sensors. Migrating sand waves and sediment transport provide a continual shifting bathymetry that is not conducive for moorings of traditional Eulerian wave buoys, while strong (tidal) currents can strain surface buoy mooring lines. Additionally, many of these tidal inlets and harbors, such as San Francisco Bay, are busy shipping ports with a steady flow of large commercial shipping.

These same challenges that make wave measurements difficult in inlets also result in strongly variable wave statistics, understanding of which is important for circulation and transport processes in the inlet, and navigation. A Lagrangian GPS drifter buoy is well-suited for the measurement of the wave field in these environments, but a modern Datawell Waverider-GPS buoy can cost as much as $14,000, making it prohibitively expensive to deploy in large numbers in an environment where one might be lost or damaged.

In this study, an inexpensive (less than $1,000) Wave Resolving Drifter (WRD) buoy developed at NPS (Herbers et al., 2012) has been improved through the use of horizontal GPS Doppler velocity measurements and the addition of a vertical-axis accelerometer. Transfer functions relating these various measurements to sea surface elevations (wave height) were applied and used to estimate the wave frequency and directional spectra observed by the buoy. These spectral estimates were then used to calculate the bulk wave statistics of the wave field.

The Doppler velocities from the GT-31 GPS receiver provide an order of magnitude improvement in the horizontal measurement over the traditional DGPS displacement measurements. An analysis was performed comparing the wave spectra and statistics from the traditional DGPS displacement measurements from the GT-31 and Doppler velocity measurements from the GT-31 to those of the well-tested Datawell DWR-G buoy. Although both GT-31 measurements provided similar statistics as the

DWR-G in the low frequency swell band; the Doppler velocity measurements agreed much better than the DGPS displacements with the Datawell estimates in the higher frequency wind wave band.

The addition of the vertical accelerometer to the WRD buoy design provided a significant improvement in the accuracy of vertical observations, which was previously lacking due to the poor vertical resolution of traditional DGPS displacement measurements. An analysis of the wave spectra and statistics demonstrates excellent agreement between the accelerometer and the DWR-G across the entire frequency band, while the traditional DGPS displacement measurements (from the GT-31) performed poorly as compared to the DWR-G.

This improved accuracy of the vertical observations allows for greater flexibility in calculating the bulk wave statistics. Previous work relied on horizontal measurements only, which yielded accurate results, but contain a 180° ambiguity in the mean wave direction (Herbers et al. 2012). The improved vertical accuracy from the accelerometer allows for the reliable use of vertical measurements as well, which removes this 180° directional ambiguity.

The validation of the WRD buoy, performed in deep water, free of any bathymetric and coastal sheltering effects, demonstrates its capability to collect robust estimates of wave spectra and statistics comparable to the industry-standard Datawell Waverider GPS buoy (DWR-G).

A large array of WRD buoys (20-30 buoys) was deployed during four cruises in and around the San Francisco Bay entrance. The buoys were well coupled to the surface current and allowed to drift out of the Golden Gate channel on the outgoing ebb current. The buoys drifted through a region of strong wave-current interactions and then over an ebb-tidal shoal, which resulted strong bathymetric effects (shoaling and refraction). Additionally, the drift tracks identify tidally-induced eddy circulations and alongshore currents near the mouth of the channel (the exit region of the tidal inlet). The spatial evolution of the wave field was analyzed on the ebb current of two deployments by

separating the time series geographically in order to statistically examine the wave field in dynamically different regions of the nearshore environment.

As the wave field propagated from offshore toward the ebb-tidal shoal, the WRD buoys observed an increase in significant wave height associated with the bathymetric interaction with the ebb-tidal shoal. The buoys also measured the distinct decrease in spectral energy in the swell band over the shoal that is likely caused by bottom friction (Pearman et al. 2013). As the wave field propagated off the shoal and into the inshore region, the buoys observed a decrease in significant wave height due to the dispersion of wave energy in the deeper water. However, they also observed some refractive effects and increased directional spreading of the wave field associated with the influence of the opposing ebb current. As the waves propagated into the channel, the buoys observed a significant decrease in significant wave height that is likely caused by a combination of the current blocking high frequency wind waves and the adjacent coastline sheltering the swell arrivals.

This study has shown that an inexpensive drifting buoy equipped with GPS and an accelerometer can provide reliable wave statistics. An array of these buoys can be used to observe the spatial and temporal evolution of a wave field in a dynamic nearshore environment. Analysis of these datasets is currently underway to study wave-current and wave-bottom interactions. The wave statistics, drift tracks and current velocities are also intended to be compared to the output of a coastal wave and circulation model for comparison. Future research is planned for deploying large arrays of these WRD buoys near the mouth of the Columbia River in Oregon later this year in order to further study wave-current interactions in the presence of tidally-enhanced river outflow.

THIS PAGE INTENTIONALLY LEFT BLANK

LIST OF REFERENCES

Andrejasic, M., 2008: MEMS Accelerometers. Seminar, 17 pp.

Barnard, P. L., D. M. Hanes, D. M. Rubin, and R. G. Kvitek, 2006: Giant sand waves at the mouth of San Francisco Bay. *EOS*, **87,** 285–289.

Brown, E., A. Colling, D. Park, J. Phillips, D. Rothery, and J. Wright, 2005: *Waves, Tides and Shallow-Water Processes*. 2nd ed. The Open University, 227 pp.

Cononmos, T. J., R. E. Smith, and J. W. Gartner, 1985: Environmental setting of San Francisco Bay. *Hydrobiologia*, **129,** 1–12.

Datawell BV, cited 2010: Datawell Waverider Reference Manual (WR-SG, DWR-MkIII, DWR-G). [Available online at http://download.datawell.nl/documentation/datawell_manual_dwr-mk3_dwr-g_wr-sg_2010–07–28.pdf.]

El-Rabbany, A., 2006: *Introduction to GPS, The Global Positioning System*. 2nd ed. Artech House, 210 pp.

Gulf Coast Data Concepts, cited 2010: USB Accelerometer Model X6–2 Specifications. [Available online at http://www.gdcataconcepts.com/GCDC-USBAccelerometerX6–2Specifications.pdf.]

Garmin Ltd., cited 2011: Astro 320 and DC40 Owner's Manual. [Available online at http://static.garmincdn.com/pumac//Astro_320_DC40_OM_EN.pdf.]

Herbers, T. H. C., P. F. Jessen, T. T. Janssen, D. B. Colbert, and J. H. MacMahn, 2012: Observing ocean surface waves with GPS-tracked buoys. *Journal of Atmospheric and Oceanic Technology*, **29,** 944–959.

Herbers, T. H. C., R. L. Lowe, and R. T. Guza, 1992: Field observations of orbital velocities and pressure in weakly nonlinear surface gravity waves. *Journal of Fluid Mechanics*, **245,** 413–435.

Krogstad, H. E. et al., 2003: Measuring and analyzing the directional spectrum of ocean waves. COST 714 Working Group 3, 200 pp.

Kuik, A. J., G. PH. Van Vledder, and L. H. Holthuijsen, 1988: A method for the routine analysis of pitch-and-roll buoy wave data. *Journal of Physical Oceanography*, **18,** 1020–1034.

Locosys Technology Inc., cited 2007: GT-31 Specifications (v1.1). [Available online at http://www.locosystech.com/product.php?id=30#.]

Long, R. B., 1980: The statistical evaluation of directional spectrum estimates derived from pitch/roll buoy data. *Journal of Physical Oceanography*, **10,** 944–952.

McWilliams, B., cited 2005: The use of CODAR high frequency radar to measure wave height with coastal buoy observation and CDIP verification in the Monterey Bay. [Available online at http://www.weather.nps.navy.mil/~psguest/OC3570/CDROM/winter2005/McWilliams/report.pdf.]

Pearman, D. W., T. H. C. Herbers, T. T. Janssen, S. A. McIntyre, and P. F. Jessen, 2013: GPS and accelerometer equipped drifters for observing ocean surface waves and currents. Draft**.**

Shi, F., D. M. Hanes, J. T. Kirby, L. Erikson, P. Barnard, and J. Eshleman, 2011: Pressure-gradient-driven nearshore circulation on a beach influenced by a large inlet-tidal shoal system. *Journal of Geophysical* Research, **116,** doi:10.1029/2010JC006788.

Stewart, R. H., cited 2008: Introduction to Physical Oceanography. [Available online at http://oceanworld.tamu.edu/resources/ocng_textbook/PDF_files/book_pdf_files.html.]

Thornton, E. B., and R. F. Krapohl, 1974: Water particle velocities measured under ocean waves. *Journal of Geophysical Research*, **79,** 847–852.

Wolf, J., and D. Prandle, 1999: Some observations of wave-current interaction. *Coastal Engineering*, **37,** 471–485.

INITIAL DISTRIBUTION LIST

1. Defense Technical Information Center
   Ft. Belvoir, Virginia

2. Dudley Knox Library
   Naval Postgraduate School
   Monterey, California